



Impact of industrial versus biomass burning aerosols on the Atlantic Meridional Overturning Circulation



Robert J. Allen¹✉, Claire Vega², Eva Yao³ & Wei Liu¹

The ocean's major circulation system, the Atlantic Meridional Overturning Circulation (AMOC), is slowing down. Such weakening is consistent with warming associated with increasing greenhouse gases, as well as with recent decreases in industrial aerosol pollution. The impact of biomass burning aerosols on the AMOC, however, remains unexplored. Here, we use the Community Earth System Model version 1 Large Ensemble to quantify the impact of both aerosol types on the AMOC. Despite relatively small changes in North Atlantic biomass burning aerosols, significant AMOC evolution occurs, including weakening from 1920 to ~1970 followed by AMOC strengthening. These changes are largely out of phase relative to the corresponding AMOC evolution under industrial aerosols. AMOC responses are initiated by thermal changes in sea surface density flux due to altered shortwave radiation. An additional dynamical mechanism involving the North Atlantic sea-level pressure gradient is important under biomass-burning aerosols. AMOC-induced ocean salinity flux convergence acts as a positive feedback. Our results show that biomass-burning aerosols reinforce early 20th-century AMOC weakening associated with greenhouse gases and also partially mute industrial aerosol impacts on the AMOC. Recent increases in wildfires suggest biomass-burning aerosols may be an important driver of future AMOC variability.

By transporting large amounts of heat, freshwater and carbon, the Atlantic Meridional Overturning Circulation (AMOC) is an important component of the climate system^{1–5}. Long-term, indirect evidence based on fingerprinting techniques supports the notion that the AMOC has weakened throughout this past century^{6–8}, including a possible transition from a strong to a weak mode⁹. Moreover, proxy records indicate the AMOC is currently in its weakest state relative to the last millennium¹⁰. Although these indirect AMOC methods have been questioned^{11–13}, a recent analysis suggests an AMOC collapse is likely to occur by mid-century¹⁴. Quantifying long-term AMOC evolution using direct observations, however, remains difficult due to natural variability^{15,16} and the relatively short (~2 decade) observational time period of the RAPID array¹⁷.

A robust feature of climate model simulations is 20th-century greenhouse gas (GHG)-induced AMOC weakening^{18–21} and aerosol-induced AMOC strengthening^{22–28}. In fact, models participating in the Coupled Model Intercomparison Project version 6 (CMIP6)²⁹ suggest aerosols dominate 20th-century AMOC evolution, although their role may be overestimated^{25–27} due for example to excessive 1960–1990 aerosol-induced

cooling³⁰. However, recent and future efforts to improve air quality through decreased aerosol emissions may weaken the AMOC^{31,32}. This implies that the 21st-century evolution of both GHGs and aerosols may reinforce one another, leading to enhanced warming and accelerated AMOC weakening.

Prior studies investigating the role of aerosols on the AMOC are based on simulations with total anthropogenic aerosol emissions (and their subsequent forcing), which includes both industrial (AER) and biomass burning (BMB) aerosols^{22–28}. This is largely due to canonical experimental designs, such as the Detection and Attribution Model Intercomparison Project (DAMIP)³³, where models are driven by total (AER and BMB) anthropogenic aerosol and precursor emissions. Although prior studies do not explicitly isolate the AMOC impacts due to AER versus BMB aerosols, some recent studies^{34–38} have found that the relatively large interannual variability associated with BMB emissions (and their aerosols) can affect longer time scale (e.g., decadal) climate variability and its mean state. For example, an increase in BMB emissions variability from 1997–2014 (due to the inclusion of satellite data) led to cloud thinning, an increase in surface solar radiation and subsequent warming of the Northern Hemisphere

¹Department of Earth and Planetary Sciences, University of California Riverside, Riverside, CA 92521, USA. ²Stockdale High School, Bakersfield, CA 93311, USA.

³Monta Vista High School, Cupertino, CA 95014, USA. ✉e-mail: rjallen@ucr.edu

(NH)³⁴. In turn, such warming of the North Atlantic is compensated by a decrease in northward oceanic heat transport associated with a weakening of the AMOC³⁸.

Here, we exploit the availability of separate AER and BMB simulations, which were conducted as part of the Community Earth System Model version 1 Large Ensemble (CESM1-LE)^{39,40}. Thus, unlike prior AMOC studies which have focused on the role of total (AER and BMB) aerosol forcing, we isolate the relative roles of each type of aerosol. We find BMB drives significant AMOC evolution, which is generally out of phase relative to the corresponding AER AMOC evolution.

Results

Description of experiments

CESM1-LE simulations (Methods) adopt the “all-but-one-forcing” experimental design, where the forcing agent/emissions of interest are held fixed at the beginning of the simulation⁴⁰. This includes a 40-member ensemble with all-forcing (ALL); a 20-member ensemble with atmospheric GHGs fixed at 1920 levels (XGHG); a 20-member ensemble with AER emissions fixed at 1920 levels (XAER); and a 15-member ensemble with BMB emissions fixed at 1920 levels (XBMB). The climate impact of the forcing agent of interest is obtained by subtracting the all-but-one-forcing simulation from the corresponding ALL simulation. In this manner, the BMB climate signal is defined as ALL–XBMB; the AER signal as ALL–XAER; and the GHG signal as ALL–XGHG. We use 20 ensemble members for ALL, GHG and AER, and 15 members for BMB. In contrast to single-forcing experiments (e.g., DAMIP), the CESM1-LE all-but-one-forcing experimental design includes nonlinear interactions (e.g., possible impacts of GHG-induced warming on aerosol-cloud interactions). Although such experimental design choices have been shown to impact the AER-forced response in CESM2-LE⁴¹ (the successor to CESM1-LE), this sensitivity to experimental design is not found in CESM1-LE⁴².

This analysis focuses on the 1920–2029 time period, as the XBMB simulations end in 2029. In the subsequent sections, time series show regional averages over two regions (depending on the variable), including the North Atlantic (30–65°N; 0–80°W; Supplementary Fig. 1a) and the subpolar North Atlantic (SPNA; 45–65°N; 0–80°W; Supplementary Fig. 1b). The larger, North Atlantic region is used to investigate the initiators of AMOC changes (e.g., drivers of AMOC trend reversals), including aerosol evolution and surface density fluxes. The SPNA region is used to quantify time series associated with AMOC feedback (since they tend to be largest in the SPNA).

AMOC Evolution

Figure 1 shows the AMOC model mean annual mean time series for ALL, GHG, AER and BMB. The AMOC is defined as the maximum stream function below 500 m at 26°N in the Atlantic Ocean¹⁷ (similar results exist for nearby latitudes). Note that the GHG, AER and BMB time series start near 0 Sverdrups ($Sv = 10^6 m^3 s^{-1}$) in 1920, as these signals are based on the difference of experiments (as discussed above). For both AER and BMB, an AMOC trend reversal occurs and their respective AMOC evolution is largely out of phase. The AER AMOC strengthens up to ~1990 and subsequently weakens, which is similar to AMOC evolution in CMIP6 models under total (AER+BMB) anthropogenic aerosol forcing³⁶. In contrast, the BMB AMOC weakens up to ~1970 and subsequently strengthens. Depth versus latitude Atlantic meridional stream function trends for AER and BMB are included Supplementary Fig. 2. Ocean mixed layer depth evolves in a similar manner as the AMOC under both BMB and AER (Supplementary Fig. 3). This includes deepening of the ocean mixed layer during the time periods of AMOC strengthening (indicative of enhanced convection) and shallowing of the ocean mixed layer (indicative of reduced convection) during the time periods of AMOC weakening.

The BMB AMOC weakening up to ~1970 is comparable to that associated with GHGs at $-0.6 Sv$ versus $-0.8 Sv$, respectively. This implies that both BMB and GHG are responsible for 1920–1960 ALL AMOC weakening (Fig. 1a). BMB has also likely (weakly) muted the 1990–2029 ALL

AMOC weakening associated with both AER and GHG. In the next section, we relate these AMOC changes (in particular the trend reversals) to corresponding evolution of North Atlantic aerosols.

Aerosol evolution

Figure 2 a, b shows model mean annual mean North Atlantic (30–65°N; 0–80°W) time series of aerosol optical depth (AOD), which represents the amount of sunlight scattered and absorbed by all aerosols, for AER and BMB. Aerosols act to cool the surface by reducing surface solar radiation through both aerosol-radiation and aerosol-cloud interactions. Such aerosol-induced cooling, largely attributed to total (BMB+AER) anthropogenic aerosol forcing, has been associated with AMOC strengthening in model simulations^{25,26}. As with the largely out-of-phase AMOC evolution under AER versus BMB, there is also a corresponding out-of-phase evolution of AOD. BMB AOD transitions from decreasing to increasing near ~1965, whereas AER AOD transitions from increasing to decreasing near ~1975. The early-period (i.e., 1920–1965) decrease in BMB AOD is related to relatively strong negative trends in the southeast U.S. and along the east coast of the U.S. and the western North Atlantic (Fig. 2d). The latter-period (i.e., 1965–2029) increase in BMB AOD is related to positive trends over the eastern North Atlantic (note also remote positive trends in the boreal forests of Canada and Russia; Fig. 2f). The corresponding AER AOD trend reversal is related to both U.S. and European emissions (Fig. 2c, e), consistent with the adoption of clean air policies.

Inspection of the North Atlantic AOD (Fig. 2) and AMOC (Fig. 1) time series shows that the AOD trend reversal for both AER and BMB precedes the corresponding AMOC trend reversal. A formal lead-lag North Atlantic AOD versus AMOC correlation analysis over the entire 1920–2029 time period shows that maximum positive correlations with AER occur when AOD leads the AMOC by ~5 years (Fig. 2g). This supports the importance of aerosols in driving AMOC changes under AER, and is consistent with prior studies^{25,26} showing that an increase in aerosols drives AMOC strengthening whereas a decrease in aerosols drives AMOC weakening (i.e., a positive correlation). AOD evolution under ALL, including North Atlantic AOD versus AMOC lead-lag correlations (maximum positive values when AOD leads AMOC by ~7–8 years) are similar to AER (Supplementary Fig. 4). The delayed AMOC response is likely related to signal propagation of subpolar North Atlantic buoyancy anomalies via Kelvin waves/boundary currents^{43–45}, which impact the AMOC in the lower latitudes (e.g., 26°N). In contrast to AER (and ALL), however, maximum positive lead-lag correlations for BMB occur when the AMOC leads AOD by ~7–8 years (Fig. 2h), suggesting a more complex relationship between AOD and the AMOC for BMB.

Another important point is that the AOD trends are much larger under AER (and ALL) as opposed to BMB (Fig. 2). For example, AER AOD changes by 0.10 to $0.20 10^{-1}$ whereas BMB AOD changes by less than $0.05 10^{-1}$ (Fig. 2a,b). Although the AER AMOC change is also larger than that under BMB (Fig. 1), this difference is considerably smaller than the corresponding AOD difference. In other words, the AMOC is more sensitive to AOD changes when those changes are due to BMB rather than AER. The regression slope ($\delta AMOC/\delta AOD$) is $34.8 Sv$ per 10^{-1} for BMB versus $10.1 Sv$ per 10^{-1} for AER (ALL also yields $10.1 Sv$ per 10^{-1}). As will be discussed below, the larger BMB regression slope ($\delta AMOC/\delta AOD$) is related to a dynamical response involving surface wind speeds and surface heat fluxes, which further promotes AMOC acceleration in the latter time period under BMB. In contrast, the dynamical response does not occur under AER.

We also note that the latter-period increase in North Atlantic BMB AOD (Fig. 2b, f) is only weakly associated with increases in anthropogenic aerosols. In general, anthropogenic aerosols include both industrial and biomass burning aerosols, and include black carbon (BC), primary organic matter (POM), sulfate (SO₄) and secondary organic aerosol (SOA). In contrast, natural aerosols (whose emissions depend on climate parameters, such as surface wind speed) include dust and sea salt (SS). Supplementary Fig. 5 shows North Atlantic time series and trend maps of anthropogenic aerosol (i.e., BC+POM+SO₄+SOA) and SS burden for BMB (we note that dust aerosol does not appear to be important). Most of the latter-period

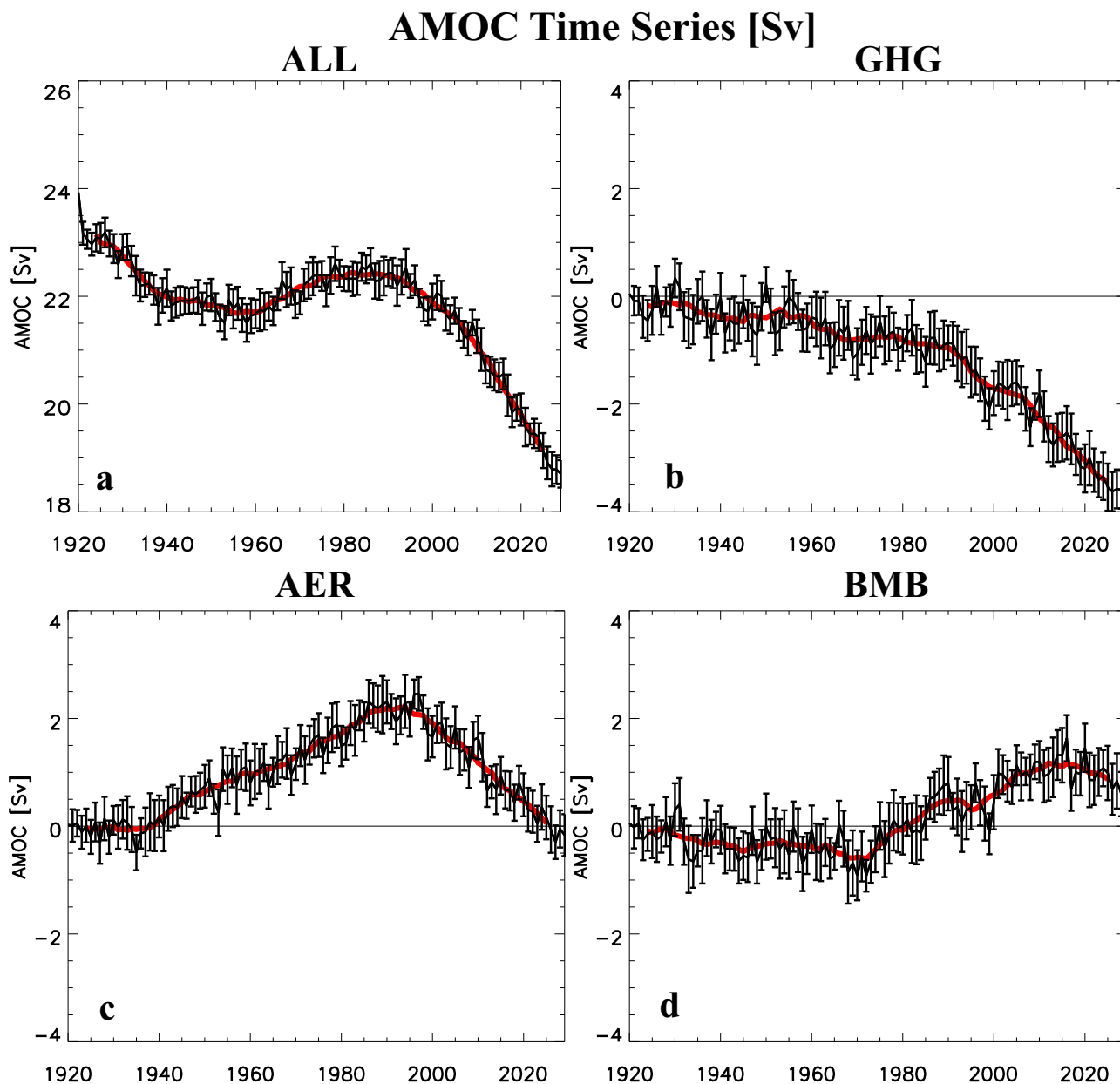


Fig. 1 | 1920-2029 AMOC time series. Model mean annual mean AMOC time series for a ALL; b greenhouse gas (GHG); c industrial aerosol (AER); and d biomass burning aerosol (BMB) forcing. Units are Sverdrups ($\text{Sv} = 10^6 \text{ m}^3 \text{ s}^{-1}$). Error bars show the 90% confidence interval. Red line shows the 9-year smoothed time series.

ALL forcing time series show absolute values; GHG, AER and BMB time series show anomalies relative to ALL (e.g., AER is estimated as ALL – XAER, where XAER is the all-but-AER-forcing simulation).

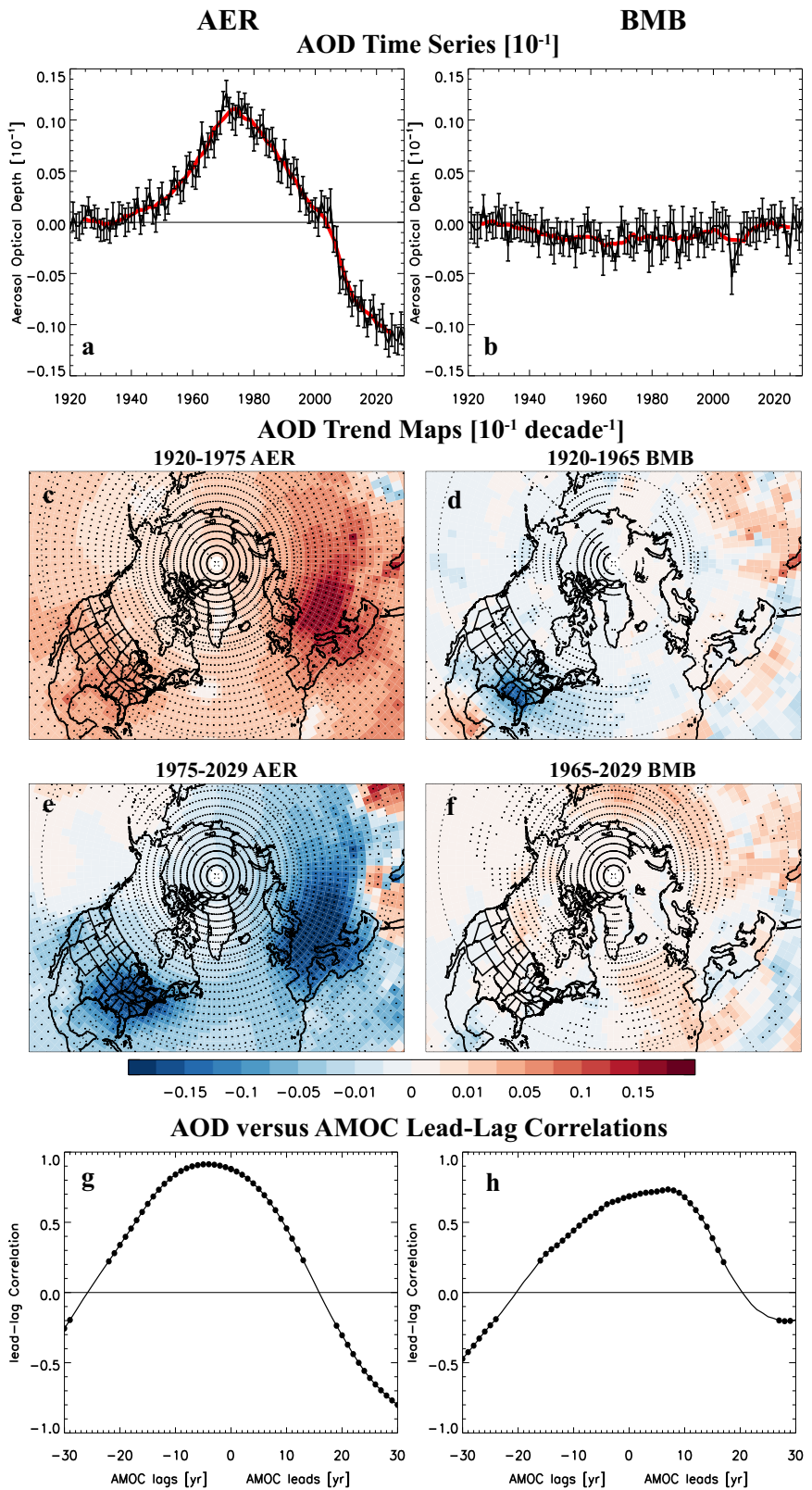
increase in North Atlantic AOD (which includes all aerosols) under BMB (Fig. 2b, f) is related to SS (as opposed to anthropogenic aerosols). Moreover, the BMB evolution of SS burden (Supplementary Fig. 5b) is similar to AMOC evolution (Fig. 1d), both of which increase during the latter time period. A lead-lag correlation analysis supports this association, as maximum North Atlantic SS burden versus AMOC lead-lag correlations occur for positive correlations when the AMOC leads the SS burden by a few years (Supplementary Fig. 5h).

This helps to explain why the maximum AOD versus AMOC BMB lead-lag correlations occur when the AMOC leads AOD (Fig. 2h). AOD includes all aerosols, so the AMOC influence on SS burden is included in the AOD versus AMOC lead-lag correlations in Fig. 2h. Thus, the latter-period increase in the AMOC under BMB is not strongly associated with increases in North Atlantic biomass burning aerosol (we return to this point in Section 2.5 Additional BMB Responses). We also note that although the

anthropogenic aerosol burden (which is not impacted by SS) versus AMOC lead-lag correlations under BMB (Supplementary Fig. 5g) indicate a reduced leading role for the AMOC (i.e., recall the AMOC clearly leads AOD; Fig. 2h), it is also the case that anthropogenic aerosols do not strongly lead the AMOC.

As with BMB versus AER North Atlantic AOD trends (Fig. 2a, b), anthropogenic aerosol burden trends under BMB (Supplementary Fig. 5) are much smaller than those under AER (Supplementary Fig. 6). Although AER also features relatively large SS burden trends (mainly in the subpolar North Atlantic, south of Iceland), the anthropogenic aerosol burden trends are considerably larger (in contrast to BMB). Similar to BMB, however, evolution of AER North Atlantic SS burden (Supplementary Fig. 6b) is similar to AER AMOC evolution (Fig. 1c). An AER lead-lag correlation analysis supports this association, as maximum North Atlantic SS burden versus AMOC lead-lag correlations occur for positive correlations near zero

Fig. 2 | Aerosol optical depth time series and spatial trend maps. The model mean annual mean aerosol optical depth (AOD) plots for **a, c, e, g** industrial aerosol (AER); and **b, d, f, h** biomass burning aerosol (BMB) forcing. North Atlantic (30–65°N; 0–80°W) 1920–2029 anomaly (i.e., ALL–XAER or ALL–XBMB) time series of AOD for **a** AER and **b** BMB. Units are 10^{-1} . Error bars show the 90% confidence interval. Red line shows the 9-year smoothed time series. Also included are the **c** 1920–1975 and **e** 1975–2029 AOD AER trend maps; and the **d** 1920–1965 and **f** 1965–2029 AOD BMB trend maps. Trend units are 10^{-1} decade $^{-1}$. Black symbols show regions where the trend is significant at the 90% confidence level, based on a standard two-tailed *t*-test. North Atlantic AOD versus AMOC lead-lag correlations are shown for **g** AER and **h** BMB. Correlations are based on the 1920–2029 model mean annual mean 9-year smoothed and detrended times series. Symbols show a significant correlation at the 90% confidence level, based on a standard two-tailed *t*-test.



lead-lag (Supplementary Fig. 6h). These AER results further suggest that changes in SS burden are in part associated with AMOC changes (i.e., a feedback). The reason why strengthening of the AMOC is associated with an increase in SS burden (and weakening of the AMOC is associated with a decrease in SS burden), under both AER and BMB, is related to enhanced poleward ocean heat transport under AMOC strengthening, warming of sea

surface temperatures, and enhanced SS emissions (discussed further in Section 2.6 AMOC Feedbacks). Moreover, part of the SS burden response under BMB (from 1960–1990) is related to a dynamical response involving a strengthened North Atlantic sea-level pressure gradient and enhanced near-surface wind speeds (Section 2.5 Additional BMB Responses), the latter of which also contributes to increased SS emissions.

Surface density fluxes

Surface density flux (SDF; Methods) indicates the loss or gain of density (buoyancy) at the ocean surface due to thermal and haline exchanges^{26,46,47}. An increase in North Atlantic SDF is associated with the strengthening of the AMOC; a decrease in SDF is associated with the weakening of the AMOC²⁶. Figure 3a, b shows the model mean annual mean time series of North Atlantic (30–65°N; 0–80°W) SDF. The evolution of the SDF closely corresponds to the AMOC (Fig. 1), indicating an increase in North Atlantic SDF is associated with AMOC strengthening, whereas a decrease in SDF is associated with AMOC weakening. Figure 3c,d shows the thermal component of SDF (TSDF), which is nearly the same as SDF, implying its importance relative to the haline component of SDF (SSDF; Fig. 3k, l). The shortwave radiation component of TSDF (TSDF_{SW}) is included in Fig. 3e,f. The AER TSDF_{SW} trend reversal near ~1970 and the BMB TSDF_{SW} trend reversal near ~1960 corresponds to the timing of the AOD trend reversal under AER and BMB, respectively (Fig. 2). Both TSDF_{SW} trend reversals also precede the corresponding SDF (and AMOC) trend reversal, suggesting that the SDF associated with surface SW radiation initiates both the SDF and AMOC trend reversals. Additional SDF components, including the sensible heat and evaporation (i.e., latent heat) TSDF are shown in Fig. 3g–j. TSDF_{EVAP} acts to offset part of TSDF_{SW} whereas TSDF_{SH} evolution is generally similar to (but weaker than) TSDF. The other SDF components are smaller (not shown). Similar conclusions apply for SDF evolution under ALL forcing (Supplementary Fig. 7), in particular the importance of TSDF_{SW} (Supplementary Fig. 7c).

Figure 4 shows lead-lag correlation plots between the AMOC and components of the SDF which support the above assertions. SDF, TSDF and TSDF_{SW} all yield significant positive correlations that lead the AMOC. For SDF and TSDF, the maximum lead-lag correlation occurs when they lead the AMOC by a few (~3–4) years. For TSDF_{SW} (Fig. 4e, f), the maximum lead-lag correlation occurs at a larger lead time (particularly for BMB). Both AER and BMB also show significant negative correlations where TSDF_{SW} (and other components, such as TSDF) lag the AMOC. Such a feature indicates an AMOC negative feedback (to be discussed below). We also note TSDF_{EVAP} under AER exhibits lead-lag AMOC correlations (Fig. 4g) that are a mirror-image of those associated with TSDF_{SW} (Fig. 4e). This supports the above finding that TSDF_{EVAP} is inversely related to TSDF_{SW}. That is, an increase in AOD leads to decreases in surface solar radiation and hence, increased TSDF_{SW}. Similarly, the decrease in surface solar radiation leads to less evaporation and decreased TSDF_{EVAP}. Under BMB, however, the maximum lead-lag correlations between TSDF_{EVAP} and AMOC occur near zero lead-lag, implying TSDF_{EVAP} and the AMOC are closely related (perhaps related to the smaller AOD changes). The lead-lag correlations between TSDF_{SH} and the AMOC (Fig. 4i,j) show maximum correlations near zero lead-lag for AER; for BMB, however, the maximum correlations occur when TSDF_{SH} leads to AMOC by a few years.

Additional BMB Responses

As mentioned above, North Atlantic AOD trends are considerably weaker under BMB as compared to AER (e.g., Fig. 2). However, the BMB AMOC response is relatively large (Fig. 1). This is particularly the case in the latter time period, when the BMB AMOC increases relatively rapidly, even though most of the AOD increase is related to increases in SS burden and not biomass burning aerosol (Supplementary Fig. 5). We suggest that this latter-period BMB AMOC increase is in part related to a dynamical mechanism.

Figure 5 a, b shows 1960–1990 trends (approximately 10 years before the BMB AMOC reversal; Fig. 1d) in sea-level pressure (SLP) and near-surface wind speed (WS) under BMB. Significant increases in WS occur, which are related to the changes in SLP, including increased SLP near western Europe and decreased SLP near Greenland and Iceland. Such an SLP pattern is reminiscent of the positive phase of the North Atlantic Oscillation (NAO), i.e., strengthening of the Azores high and deepening of the Icelandic low. A prior analysis found a somewhat similar SLP pattern

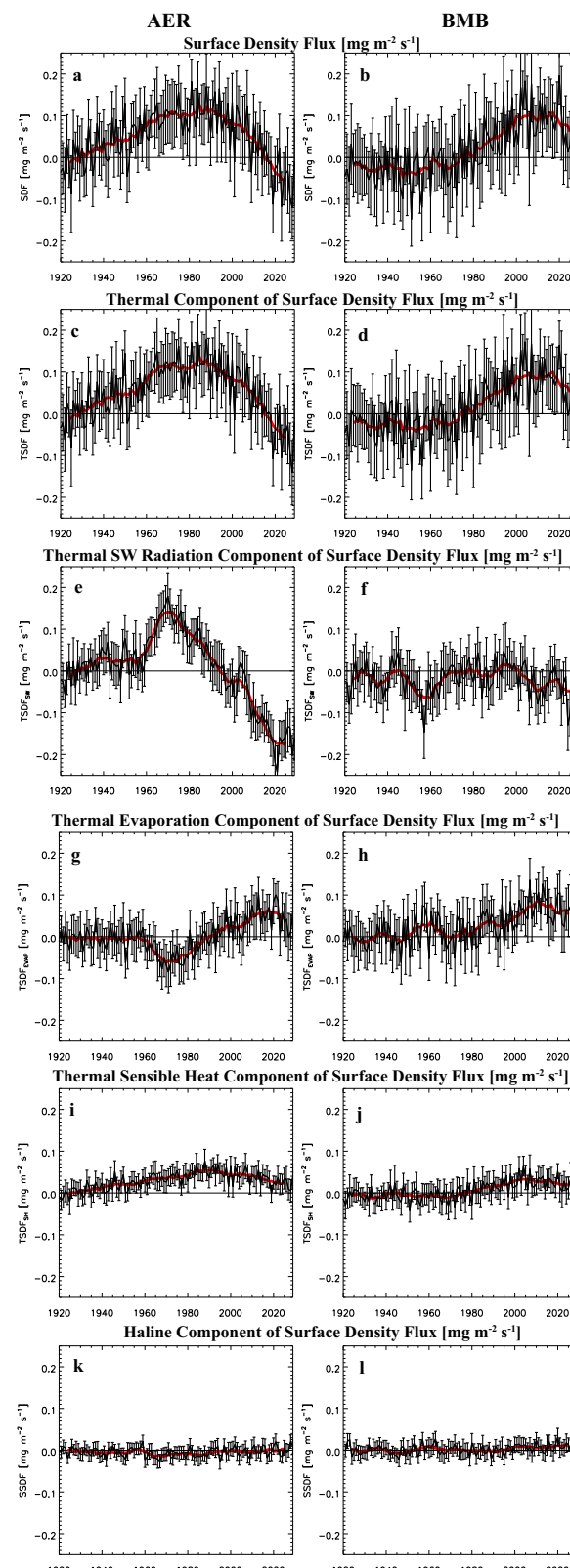
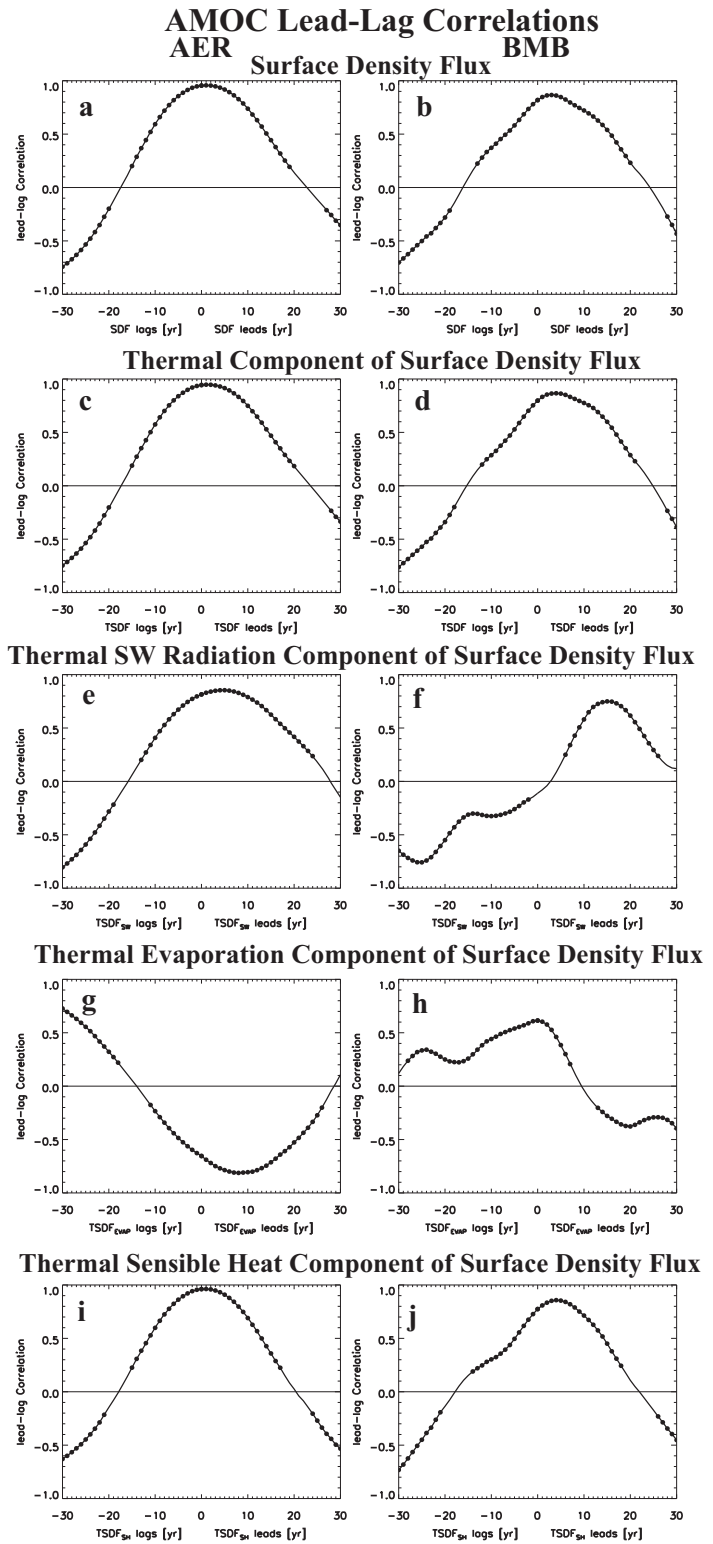


Fig. 3 | 1920–2029 surface density flux time series. Model mean annual mean North Atlantic (30–65°N; 0–80°W) anomaly (i.e., ALL–XAER or ALL–XBMB) time series under **a**, **b**, **c**, **d**, **f**, **h**, **j**, **l** biomass burning aerosol (BMB) forcing for **a**, **b** surface density flux (SDF); **c**, **d** thermal component of SDF (TSDF); **e**, **f** shortwave radiation component of TSDF (TSDF_{SW}); **g**, **h** evaporation component of TSDF (TSDF_{EVAP}); **i**, **j** sensible heat component of TSDF (TSDF_{SH}); and **k**, **l** haline component of SDF (SSDF). Units are $\text{mg m}^{-2} \text{s}^{-1}$. Error bars show the 90% confidence interval. The red line shows the 9-year smoothed time series.

Fig. 4 | Lead-lag AMOC correlation plots. Model mean lead-lag correlation plots under **a, c, e, g, i** industrial aerosol (AER) and **b, d, f, h, j** biomass burning aerosol (BMB) forcing between the AMOC and **a, b** surface density flux (SDF); **c, d** thermal component of SDF (TSDF); **e, f** shortwave radiation component of TSDF (TSDF_{SW}); **g, h** evaporation component of TSDF (TSDF_{EVAP}); and **i, j** sensible heat component of TSDF (TSDF_{SH}). Correlations are based on the annual mean 9-year smoothed and detrended North Atlantic (30–65°N; 0–80°W) SDF and AMOC time series. Symbols show a significant correlation at the 90% confidence level, based on a standard two-tailed *t*-test.



under total (AER+BMB) aerosols²⁶. Furthermore, several studies have found a connection between the NAO and the AMOC^{48–50}, with a positive NAO leading to a stronger AMOC by extracting heat from the subpolar gyre. Similarly, several studies have found that anthropogenic aerosols, through heterogeneous heating/cooling and the generation of Rossby waves^{51–54}, can trigger atmospheric teleconnection (e.g., remote SLP perturbations). Although we do not pursue this farther here, we note the bulk of the 1960–1990 BMB anthropogenic aerosol burden increase occurs over Canada (Fig. 5i), which corresponds to relatively large surface cooling (Fig.

5e). Moreover, the subpolar North Atlantic SLP and WS trends maximize during the winter season, when the NAO exhibits its largest variability, and the propagation of Rossby waves is favored.

The increase in WS promotes an increase in latent and sensible cooling and an increase in the corresponding TSDFs (Fig. 5c, d). We suggest this dynamic mechanism contributes to the AMOC increase under BMB from 1960–1990. We also note that the increase in WS (Fig. 5b) also promotes an increase in SS burden (Fig. 5f) through enhanced SS emissions (subpolar North Atlantic warming associated with AMOC strengthening is relatively

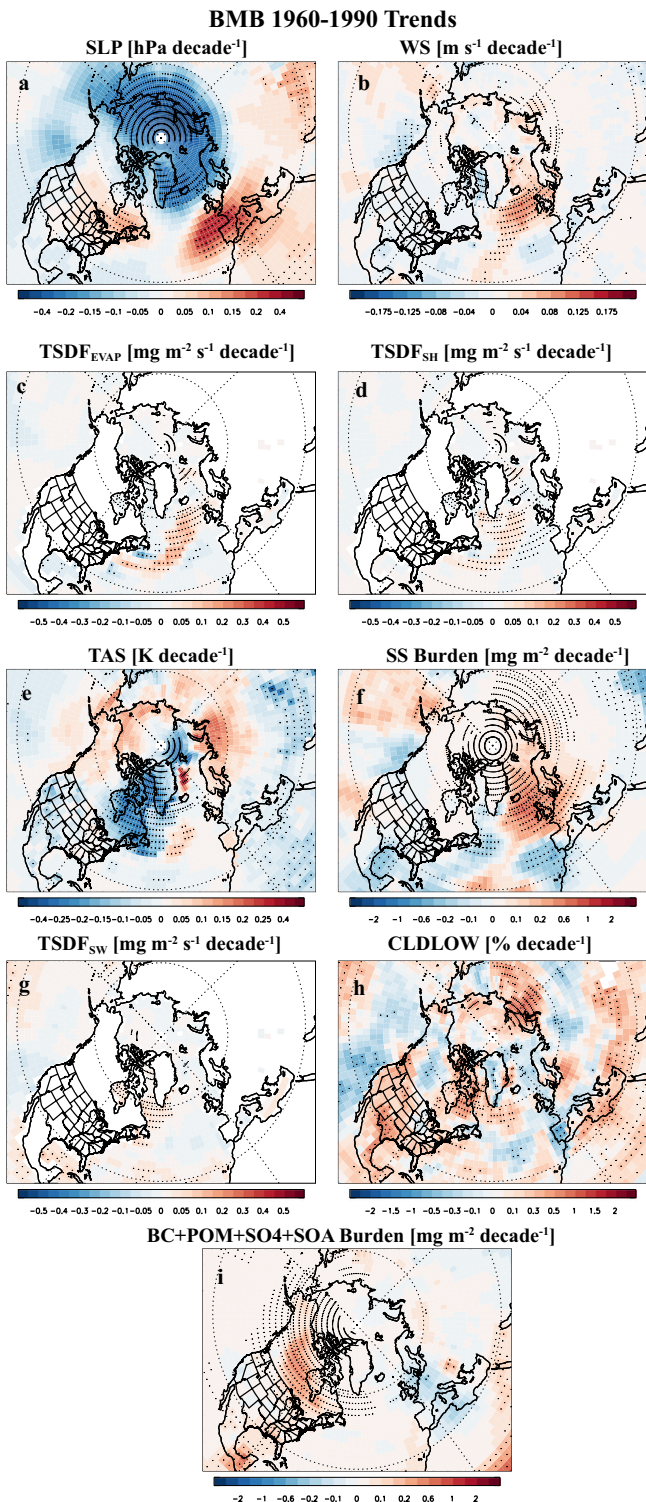


Fig. 5 | 1960–1990 BMB trend maps. 1960–1990 BMB **a** sea-level pressure (SLP; [hPa decade^{-1}]); **b** near-surface wind speed (WS; [$\text{m s}^{-1} \text{ decade}^{-1}$]); **c** thermal evaporation component of surface density flux (TSDF_{EVAP}; [$\text{mg m}^{-2} \text{ s}^{-1} \text{ decade}^{-1}$]); **d** thermal sensible heat component of surface density flux (TSDF_{SH}; [$\text{mg m}^{-2} \text{ s}^{-1} \text{ decade}^{-1}$]); **e** near-surface air temperature (TAS; [K decade^{-1}]); **f** sea salt burden (SS; [$\text{mg m}^{-2} \text{ decade}^{-1}$]); **g** thermal shortwave radiation component of surface density flux (TSDF_{SW}; [$\text{mg m}^{-2} \text{ s}^{-1} \text{ decade}^{-1}$]); **h** low cloud cover (CLDLOW; [% decade $^{-1}$]); and **i** anthropogenic aerosol (BC+POM+SO₄+SOA; [$\text{mg m}^{-2} \text{ decade}^{-1}$]) burden trends. Black symbols show regions where the trend is significant at the 90% confidence level, based on a standard two-tailed *t*-test.

weak over this time period and likely less important, Fig. 5e). Thus, the increase in WS helps to explain the SS burden increase under BMB in the latter-time period (i.e., Supplementary Fig. 5b).

To further support the importance of this dynamical mechanism to BMB AMOC changes, Fig. 6 shows lead-lag correlation plots between the SLP gradient (dSLP) and several variables. dSLP is defined as 30–50°N and 0–60°W minus 60–90°N; 0–60°W (Supplementary Fig. 1c). Thus, an increase in dSLP is associated with the SLP pattern noted above (Fig. 5a), including increased SLP near the Azores and decreased SLP near Iceland. The first thing to note is that maximum lead-lag correlations between dSLP and the AMOC occur with dSLP leading the AMOC by ~5 years. As this correlation is positive, it is consistent with increased dSLP leading an increase in the AMOC (through the aforementioned increases in WS and TSDF). Furthermore, Fig. 6b shows dSLP and WS lead-lag correlations peak at 0 lead-lag, suggesting that the change in near-surface wind speed is directly related to the altered pressure gradient (i.e., an increase in dSLP is associated with an increase in WS). Finally, Fig. 6c,d shows dSLP and both TSDF and TSDF_{SH} exhibit maximum (positive) lead-lag correlations near 0 lead-lag. This supports the importance of the increased near-surface wind speed to corresponding increases in both TSDF and TSDF_{SH}, which in turn promote AMOC strengthening. This mechanism also implies that TSDF, and in particular TSDF_{SH} lead the AMOC under BMB, which is supported in Fig. 4d,j. Although the 1960–1990 increase in TSDF_{EVAP} (Fig. 5c) is also associated with the enhanced dSLP and WS, the dSLP versus TSDF_{EVAP} lead-lag correlations (over the entire 1920–2029 time period) do not exhibit maximum correlations near 0 lead-lag (as was the case between dSLP versus TSDF and TSDF_{SH}). Instead, the dSLP versus TSDF_{EVAP} lead-lag correlations (Fig. 6e) are nearly identical to the dSLP versus AMOC lead-lag correlations (Fig. 6a), implying the importance of the AMOC to TSDF_{EVAP} (i.e., Fig. 4h shows AMOC and TSDF_{EVAP} BMB correlations are maximum at 0 lead-lag) over the entire time period.

The BMB AMOC continues to increase post-1990 (through about 2020; Fig. 1d). The 1990–2020 BMB SLP and WS trends in the North Atlantic are negligible (ruling out the continued importance of the dynamical mechanism). Similarly, anthropogenic aerosol (BC+POM+SO₄+SOA) burden trends are negligible (most of the 1990–2020 increase occurs over Russia; Fig. 7i). As opposed to the dynamical mechanism previously described (as well as direct anthropogenic aerosol forcing), this continued AMOC strengthening appears to be related to an AMOC-induced increase in ocean salinity flux convergence (Section 2.7 Ocean Salinity & Heat Budgets). Figure 7a, b shows increases in the subpolar North Atlantic sea surface density (ρ), all of which is due to an increase in the salinity component, ρ_s (the thermal component, ρ_T weakly decreases). This increase in sea surface density promotes enhanced convection. Continued BMB AMOC strengthening post-1990 is also likely related to an enhanced poleward ocean heat transport (associated with a stronger AMOC) and surface warming (Fig. 7e). Similarly, relatively large TSDF_{EVAP} (Fig. 7c) and SS burden increases (Fig. 7f) occur, in nearly the same location as the warming. The former promotes denser surface water and continued AMOC strengthening. As previously noted, this also implies that TSDF_{EVAP} and the AMOC are in phase (near 0 lead-lag positive correlation; Fig. 4h).

Although the increase in SS burden (Fig. 7f) should also promote AMOC strengthening via reducing surface solar radiation and increasing TSDF_{SW}, this is overwhelmed (i.e., TSDF_{SW} decreases; Fig. 7g) by relatively large decreases in low cloud cover (CLDLOW; Fig. 7h). The CLDLOW decrease also largely occurs where the surface warms, again suggesting that this response is associated with enhanced poleward ocean heat transport and surface warming related to the stronger AMOC (discussed further in Section 2.6 AMOC Feedbacks).

AMOC Feedbacks

We have argued that AER and BMB AMOC variations are largely initiated by changes in the North Atlantic SDF, and in particular aerosol induced

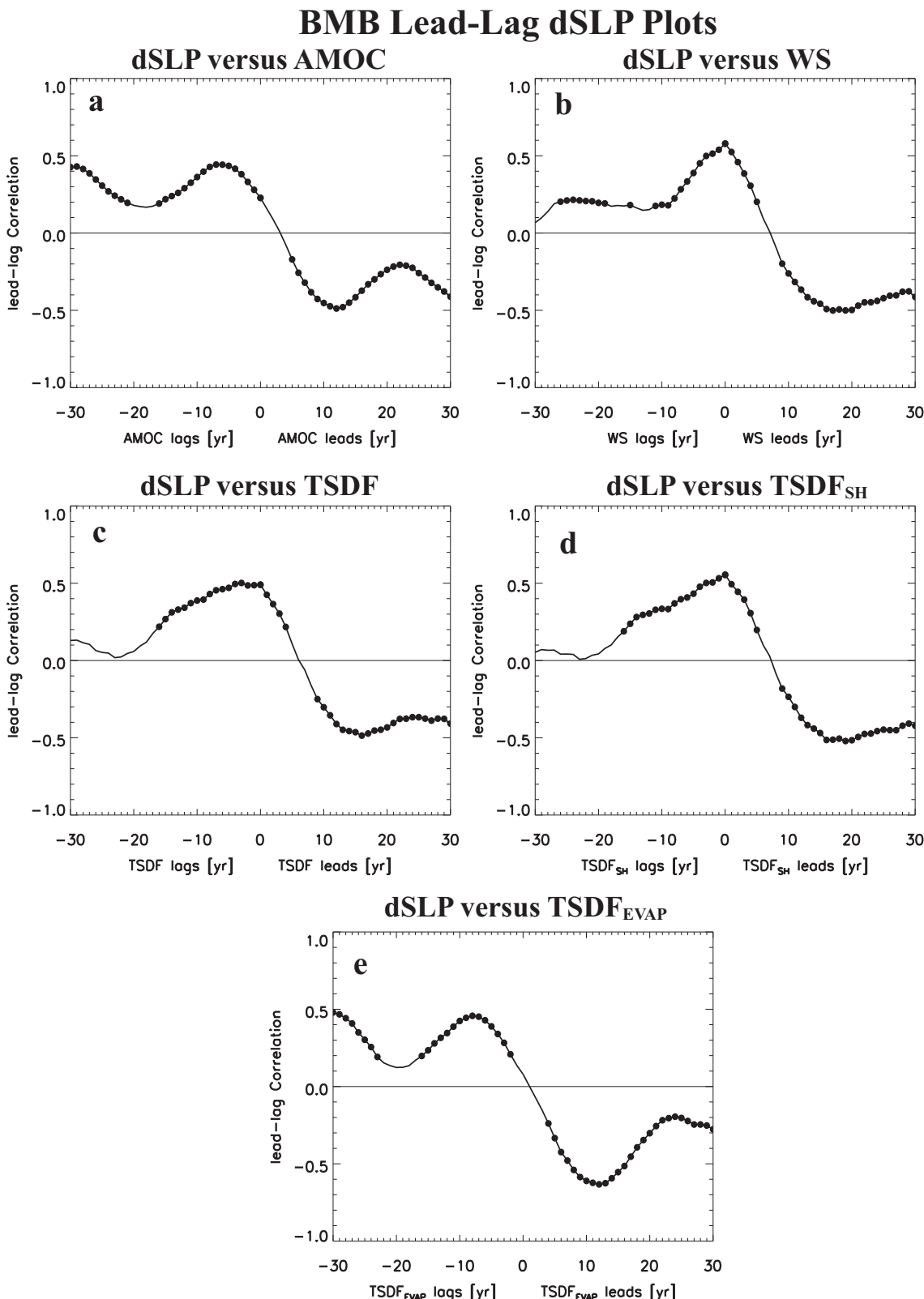


Fig. 6 | Lead-lag sea-level pressure gradient (dSLP) correlation plots under BMB. Model mean lead-lag correlation plots under biomass burning aerosol (BMB) forcing between the sea-level pressure gradient (dSLP; 30–50°N and 0–60°W minus 60–90°N; 0–60°W) and **a** AMOC; **b** near-surface wind speed (WS); **c** thermal component of the surface density flux (TSDF); **d** thermal sensible heat component of

SDF (TSDF_{SH}); and **e** thermal evaporation component of SDF (TSDF_{EVAP}). Correlations are based on the annual mean 9-year smoothed and detrended time series (over the subpolar North Atlantic for WS, TSDF, TSDF_{SH} and TSDF_{EVAP}). Symbols show a significant correlation at the 90% confidence level, based on a standard two-tailed *t*-test.

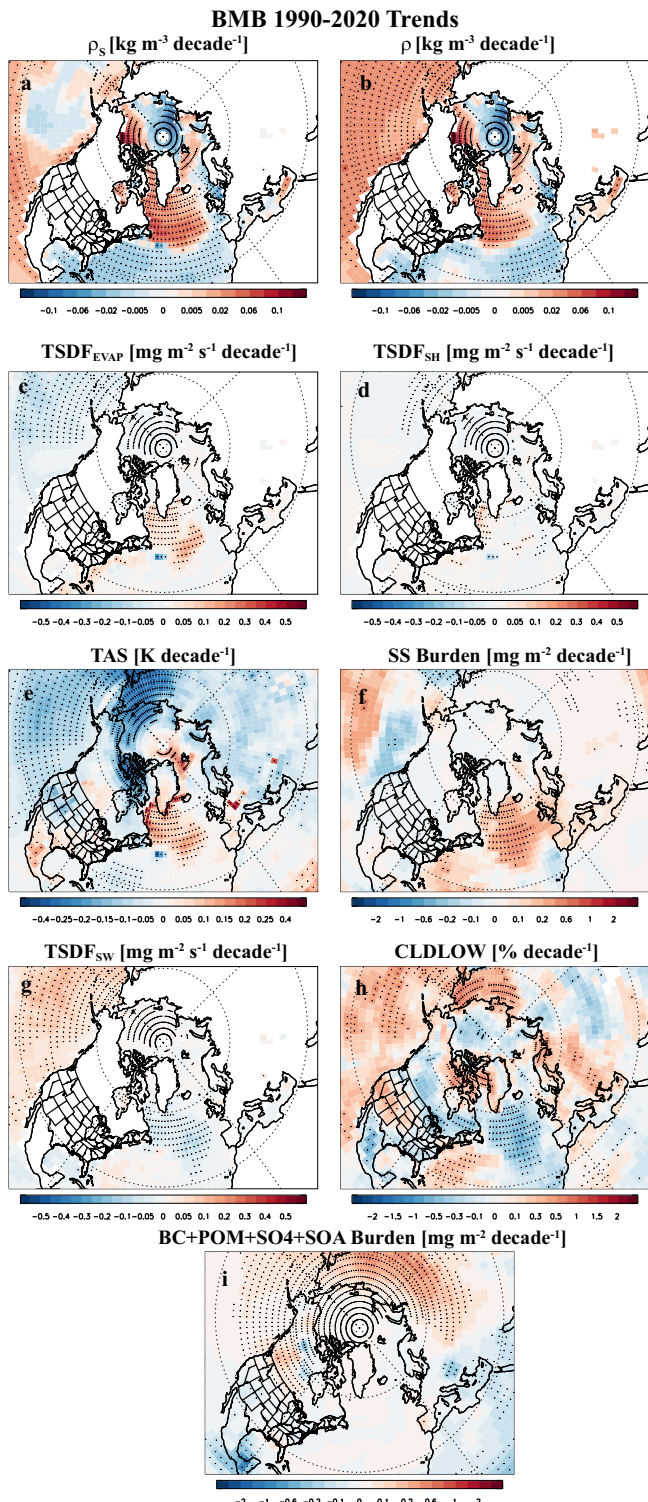


Fig. 7 | 1990–2020 BMB trend maps. 1990–2020 BMB **a** sea surface density due to salinity (ρ_s ; $\text{kg m}^{-3} \text{ decade}^{-1}$); **b** sea surface density (ρ ; $\text{kg m}^{-3} \text{ decade}^{-1}$); **c** thermal evaporation component of surface density flux ($\text{TSDF}_{\text{EVAP}}$; $\text{mg m}^{-2} \text{ s}^{-1} \text{ decade}^{-1}$); **d** thermal sensible heat component of surface density flux (TSDF_{SH} ; $\text{mg m}^{-2} \text{ s}^{-1} \text{ decade}^{-1}$); **e** near-surface air temperature (TAS; K decade^{-1}); **f** sea salt burden (SS; $\text{mg m}^{-2} \text{ decade}^{-1}$); **g** thermal shortwave radiation component of surface density flux (TSDF_{SW} ; $\text{mg m}^{-2} \text{ s}^{-1} \text{ decade}^{-1}$); **h** low cloud cover (CLDLOW; $\%$ decade^{-1}); and **i** anthropogenic aerosol (BC + POM + SO₄ + SOA; $\text{mg m}^{-2} \text{ decade}^{-1}$) burden trends. Black symbols show regions where the trend is significant at the 90% confidence level, based on a standard two-tailed *t*-test.

changes in surface SW radiation and TSDF_{SW} (especially for AER). Under AER, North Atlantic AOD changes are quite large (Fig. 2a) and changes in SDF are largely due to changes in TSDF_{SW} (Fig. 3e). Under BMB, however, North Atlantic AOD changes are much smaller (Fig. 2b) and changes in SDF are due to both changes in TSDF_{SW} (Fig. 3f), as well as dynamical changes (e.g., Figs. 5, 6) and AMOC feedbacks (Fig. 7) during the latter time periods.

As mentioned above, SDF can drive the AMOC, but it can also respond to the AMOC. We use the methodology developed in ref. 26, where the AMOC feedback is isolated from the aerosol forced signal (Methods). Briefly, the 1920–2029 smoothed and detrended annual mean AMOC time series is regressed onto the various fields (e.g. SST) after first removing variability associated with the aerosol forcing (i.e., BC+POM+SO₄+SOA burden).

Figure 8 illustrates such AMOC feedbacks on surface temperature (SST), CLDLOW, TSDF_{SW} and SS burden. A stronger AMOC is associated with surface temperature warming (i.e., the regression slope, or “sensitivity” is positive) south/southeast of Greenland in all three experiments (Fig. 8a–c). A stronger AMOC is also associated with a decrease in subpolar North Atlantic low cloud cover (Fig. 8d–f). The warming is consistent with enhanced poleward ocean heat transport due to a stronger AMOC (which is evaluated below). The low cloud decrease is consistent with surface warming, which favors a reduced lower-tropospheric temperature gradient (i.e., reduced lower-tropospheric stability)^{55,56}. Furthermore, the negative AMOC-low cloud sensitivity corresponds to a negative AMOC- TSDF_{SW} sensitivity (particularly for both BMB and ALL). That is, a stronger AMOC is associated with warming SSTs, decreased low cloud cover, and increased surface shortwave radiation (i.e., decreased TSDF_{SW}) southeast of Greenland. The AMOC feedback on TSDF_{SW} acts to mute (if not offset) the direct aerosol-forced TSDF_{SW} response. Furthermore, all three experiments show that a stronger AMOC is associated with an increase in SS burden (Fig. 8g–l), largely in the subpolar North Atlantic to the south of Iceland. Such a feedback, as previously noted, is consistent with warming SSTs and enhanced SS emissions. The importance of SS burden to AOD changes under BMB was previously noted (e.g., Supplementary Fig. 5).

We reiterate that more conventional AMOC feedbacks exist, including positive feedback between the AMOC and surface turbulent heat fluxes. For example, warming SSTs (e.g., south of Greenland) under a stronger AMOC are also associated with increases in sensible and latent heat fluxes, which act to cool SSTs and increase $\text{TSDF}_{\text{EVAP}}$ and TSDF_{SH} (Supplementary Fig. 8a–f). These positive feedbacks dominate the overall feedback between the AMOC and TSDF (which is positive). Similar to ref. 26, we also note that all three experiments show that a stronger AMOC is associated with decreased SLP near Greenland/Iceland (Supplementary Fig. 8g–j) and increases in near-surface wind speed in the subpolar North Atlantic (Supplementary Fig. 8j–l). Increased subpolar North Atlantic WS also likely promotes the increases in the turbulent heat fluxes (and corresponding TSDFs) and SS burden associated with a stronger AMOC.

In Section 2.4 Surface Density Fluxes, we showed that SDF is largely dictated by TSDF, with minor contributions from SSDF (e.g., Fig. 3). SSDF, however, only captures the surface processes that impact sea surface salinity (e.g., precipitation, evaporation, ice melt). For example, the dominant component of SSDF over the subpolar North Atlantic (SPNA) in all three experiments is the ice melt component, which is partially compensated by the evaporation component (other SSDF components are small; not shown). SSDF, however, does not include changes in salinity transport and mixing by the ocean. In addition to poleward ocean heat transport, the AMOC also transports salt poleward. Thus, the expectation is that strengthening of the AMOC will result in increased North Atlantic sea surface salinity and a corresponding increase in the salinity component of sea surface density, ρ_s . A weakening of the AMOC, however, will yield a corresponding decrease in ρ_s . In other words, since surface processes are not a dominant driver of North Atlantic salinity changes in these experiments, any salinity changes are likely related to an AMOC feedback (i.e., a positive salt advection feedback^{57,58}).

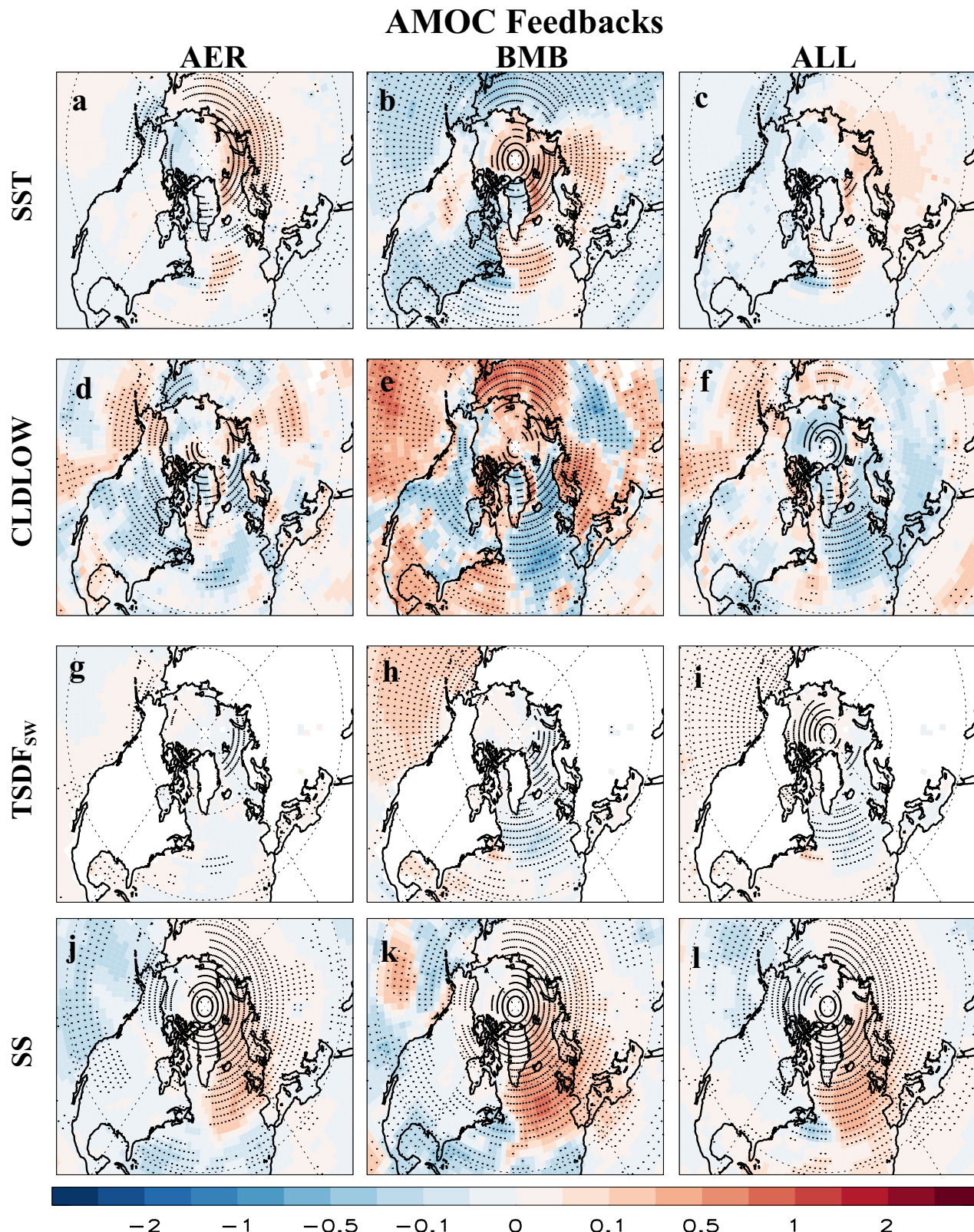


Fig. 8 | AMOC feedbacks. Model mean annual mean AMOC feedback under **a, d, g, j** industrial aerosol (AER); **b, e, h, k** biomass burning aerosol (BMB); and **c, f, i, l** ALL forcing for **(a–c)** sea surface temperature (SST); **d–f** low cloud cover (CLDLOW); **g–i** thermal shortwave radiation component of the surface density flux (TSDF_{sw}); and **(j–l)** sea salt burden (SS). The AMOC feedback is estimated by regressing the 1920–2029 annual mean 9-year smoothed and detrended AMOC time

series onto the various fields (e.g. SST) after first removing variability associated with the aerosol forcing (i.e., BC + POM + SO₄ + SOA burden). Symbols show a significant regression at the 90% confidence level, based on a standard two-tailed *t*-test. Units are K Sv⁻¹ for **a–c**; % Sv⁻¹ for **d–f**; mg m⁻² s⁻¹ Sv⁻¹ for **g–i**; and mg m⁻² Sv⁻¹ for **j–l**.

Supplementary Figs. 9–11 show analyses that support these ideas. In particular, all three forcings (AER, BMB and ALL) yield significant positive $\delta\rho_s/\delta\text{AMOC}$ sensitivities (Supplementary Figs. 9–11c) from $\sim 45^\circ\text{N}$ to 65°N and $0\text{--}80^\circ\text{W}$ (i.e., the SPNA). Time series of ρ_s over this region (Supplementary Figs. 9–11a) show significant multi-decadal variability that resembles that present in the AMOC, implying the two are closely related. We note that this is less true for the thermal component of sea surface density (ρ_T ; Supplementary Figs. 9–11b), which generally follows the evolution of aerosol forcing, but less so in the SPNA (relative to the larger North Atlantic region). This is because aerosol impacts on SSTs in the SPNA are muted by the previously discussed AMOC SST feedback.

Lead-lag correlations between the AMOC and SPNA ρ_s (Supplementary Figs. 9–11g) show maximum (positive) correlations near 0 lead-lag, but with a tendency for ρ_s to lag the AMOC (especially for BMB). Thus, a stronger AMOC is associated with an increase in SPNA salinity and ρ_s , and this increase in ρ_s is likely driven by the stronger AMOC. Similarly, a weaker AMOC is associated with a decrease in SPNA salinity and ρ_s , and this decrease in ρ_s is likely driven by the weaker AMOC. In contrast, maximum lead-lag correlations between the AMOC and SPNA ρ_T (Supplementary Figs. 9–11h) occur for positive correlations with ρ_T leading the AMOC by \sim decade or longer. This again supports the role of aerosols in initiating AMOC variability, in particular the AMOC trend reversals emphasized in this paper, by modifying SST through changes in surface solar radiation. The AMOC-SST feedback is also apparent here, as a secondary maximum (here, for negative correlations) occurs with ρ_T lagging the AMOC. These negative correlations are indicative of enhanced poleward ocean heat transport under a stronger AMOC, which eventually drives SPNA warming and a decrease in ρ_T . Similarly, these negative correlations are indicative of reduced poleward ocean heat transport under a weaker AMOC, which eventually drives SPNA cooling and an increase in ρ_T . As mentioned above, such an AMOC-SST feedback acts to mute the direct forcing from the aerosols. That is, aerosol cooling of SSTs drives a stronger AMOC (via decreased SW radiation and enhanced TSDF_{SW}), but the stronger AMOC eventually drives warming SSTs (especially southeast of Greenland) through enhanced poleward ocean heat transport. Under AER and ALL, these negative ρ_T versus AMOC correlations take more than a decade or two to become significant, with maximum (negative) correlations near 30+ years. In contrast, they are significant near zero lead-lag under BMB, with maximum (negative) values near 7–8 years (Supplementary Fig. 10h). This again supports more pronounced impacts of AMOC feedbacks under BMB, which is again likely related to the weaker BMB aerosol forcing.

Ocean salinity and heat budgets

To better understand the role of salinity in the AMOC evolution discussed here, we conduct a SPNA salinity budget analysis for the upper 100 m (see Methods; similar results also exist for the upper 200 m). Figure 9a,b shows the annual mean model mean SPNA anomaly time series of the salinity budget components, including 3D ocean salinity flux convergence by the resolved Eulerian mean flow (OSFC), horizontal diffusion (SHDIF), vertical mixing (SVMIX) as well as the surface salinity flux (SSF; which is related to SSDF) and ocean salinity (S). Increasing values for the salinity budget components indicate an increase in the ocean salinity tendency ($\frac{\partial S}{\partial t}$) over the ocean volume (SPNA region down to 100 m depth). Equivalently, decreasing values for the salinity budget components indicate a decrease in the ocean salinity tendency. Consistent with the SSDF analysis (e.g., Fig. 3k, l), changes in SSF are relatively small. Similarly, evolution of SHDIF and SVMIF generally diverge from S. OSFC, however, shows similar evolution as S (and the AMOC; Fig. 1), implying OSFC is a dominant driver of changes in S. Similar results exist for ALL (Supplementary Fig. 12a).

Our interpretation of these results is that an increase in SPNA S is largely due to an increase in OSFC, with partial compensation from SVMIX and SHDIF (i.e., some of the increased salinity is vertically mixed downwards below 100 m and horizontally diffused outside the SPNA). Similarly, a decrease in SPNA salinity is largely due to a decrease in OSFC, with partial compensation from SVMIX and SHDIF (i.e., salinity is vertically mixed

upwards and horizontally diffused inside the SPNA). A lead-lag correlation analysis shows significant positive correlations between OSFC and AMOC that peak near zero lead-lag (Supplementary Fig. 13), which reinforces the close connection between the AMOC and OSFC, as well as S. Thus, we conclude that changes in SPNA salinity are largely due to OSFC via a positive AMOC feedback, and are not a dominant initiator of the AMOC changes emphasized here. Note, however, that increases in OSFC and SPNA salinity (i.e., ρ and ρ_s) are important for continued AMOC strengthening under BMB from 1990–2020 (as discussed in Section 2.5 Additional BMB Responses).

Figure 9 c, d shows the corresponding SPNA ocean heat budget analysis, including 3D ocean heat flux convergence by the resolved Eulerian mean flow (OHFC), horizontal diffusion (HHDIF), vertical mixing (HVMIX) as well as the surface heat flux (SHF; which is related to TSDF) and ocean temperature (T). All of our heat budget components have been converted from heat/solar fluxes to temperature fluxes (Methods), and therefore have units (after converting s^{-1}) of Kyr^{-1} . Increasing values for the heat budget components indicate an increase in heat storage (i.e., temperature) in the ocean volume (SPNA region down to 100 m depth). Similarly, decreasing values for the heat budget components indicate a decrease in heat storage. Here, SPNA SHF exhibits relatively large variability (in contrast to SSF), as does both HVMIX and OHFC (HHDIF exhibits relatively small variability). OHFC variations, as with OSFC, once again resemble AMOC variability (e.g., Fig. 1). SHF and HVMIX variations are largely in opposition (with SHF dominant, however), implying heating from increases in SHF is in part vertically mixed downwards outside the SPNA volume (i.e., below 100 m). Similarly, cooling from decreases in SHF is partially offset by vertical mixing of heat from below. Thus, we conclude that changes in SPNA ocean temperature are largely related to both SHF (largely due to changes in aerosols and surface solar radiation) and OHFC related to the AMOC (which, as previously mentioned, can also impact SHF).

A lead-lag correlation analysis shows significant positive correlations between OHFC and AMOC that peak near zero lead-lag (Supplementary Fig. 14), which reinforces the close connection between the AMOC and OHFC (and with the previously discussed positive $\delta\text{SST}/\delta\text{AMOC}$ sensitivities southeast of Greenland). Thus, we conclude that changes in SPNA temperature are largely related to both surface heat fluxes and OHFC (via AMOC-related heat transport).

Discussion

Our results are limited in that we use a single climate model. However, as mentioned above, CESM1-LE yields 20th century AMOC evolution that is similar to that based on other models, including those participating in CMIP6^{25,26}. We also note that our results are based on CMIP5 emissions⁵⁹, which may differ from those in CMIP6. For example, global CMIP5 biomass burning emissions show a gradual decrease from 1920 to ~ 1950 and then a steady increase thru 2000. In contrast, CMIP6 biomass burning emissions⁶⁰ increase only slightly over the 20th century, peaking during the 1990s and then they gradually decrease. CMIP5 emissions are over a decade old and are subject to considerable uncertainties. For example, uncertainties in regional emissions can be expected to be as large as a factor of 2 (or even larger)⁵⁹. We also note that CMIP5 emissions are decadal (i.e., the model interpolates in between adjacent decades to resolve annual, but seasonally varying, emissions). Given recent studies that show the importance of interannual BMB variability to aspects of simulated decadal climate variability^{34–38}, the decadal-time scale of CMIP5 emissions adds additional uncertainty. Although beyond the scope of this analysis, we note that CESM2-LE⁴¹ (the successor to CESM1-LE) yields generally similar 1920–2029 BMB AMOC evolution as found here based on CESM1-LE, in particular AMOC strengthening from ~ 1970 onwards.

Despite the above caveats, we have shown biomass burning aerosols can drive significant changes in the AMOC (Fig. 1), despite relatively small changes in North Atlantic AOD (Fig. 2). BMB AMOC changes are initiated through altered North Atlantic surface solar radiation, which impact the thermal component of the surface density flux (i.e., TSDF_{SW}; Fig. 3), largely

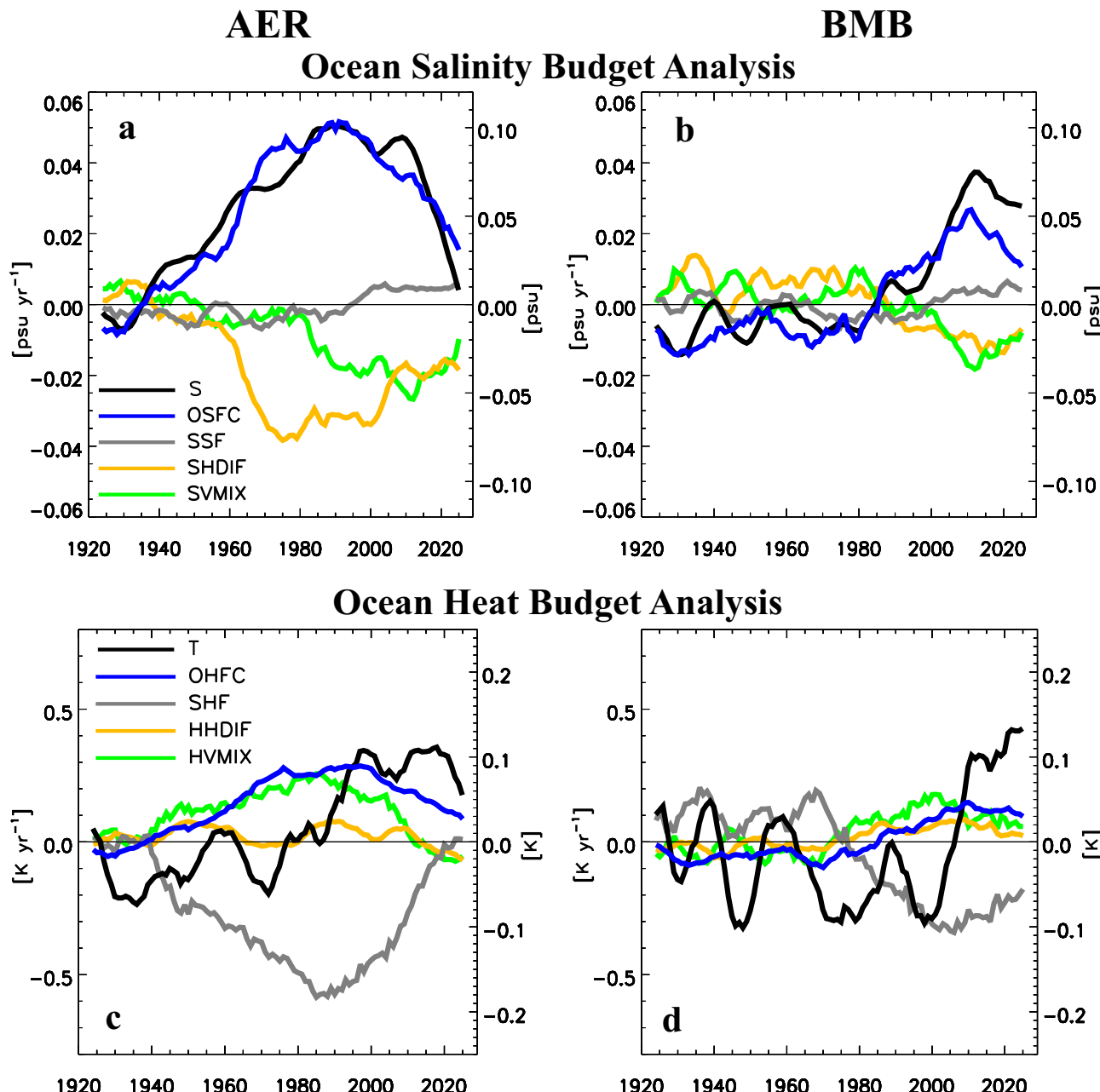


Fig. 9 | Ocean salinity and heat budget analysis. Model mean annual mean subpolar North Atlantic ($45\text{--}65^\circ\text{N}$; $0\text{--}80^\circ\text{W}$) anomaly (relative to 1920–2029) time series of ocean **a**, **b** salinity and **c**, **d** heat budgets under **a**, **c** industrial aerosol (AER) and **b**, **d** biomass burning aerosol (BMB) forcing. Salinity budget components include ocean salinity (S; black), salinity flux convergence (OSFC; blue), surface salinity flux (SSF; gray), horizontal diffusion (SHDIF; gold), and vertical mixing (SVMIX; green). Heat budget components (which have been converted from heat/solar fluxes to

temperature fluxes) include ocean temperature (T; black), heat flux convergence (OHFC; blue), surface heat flux (SHF; gray); horizontal diffusion (HHDIF; gold), and vertical mixing (HVMIX; green). Only 9-year smoothed time series are included. Budget components are based on vertical integration to a depth of 100 m. Units of S are practical salinity units (psu ; right y-axis) and units of remaining salinity budget terms are psu yr^{-1} (left y-axis). Units of T are K (right y-axis) and units of remaining heat budget terms are K yr^{-1} (left y-axis).

during the first time period (i.e., 1920–1965). AMOC strengthening from 1970 onwards (largely up to 1990; Fig. 5) is related to a dynamical mechanism, involving increased subpolar North Atlantic sea-level pressure gradient and near-surface wind speed, which increases TSDF_{EVAP} and TSDF_{SH} . Continued AMOC strengthening (post-1990; Fig. 7) is related to a positive AMOC-ocean salinity flux convergence feedback (i.e., OSFC; Fig. 9) involving an increase in sea surface density due to increased salinity (i.e., ρ_s). AMOC-induced changes in poleward ocean heat transport (i.e., OHFC; Fig. 9) also contributes through SPNA warming and enhanced TSDF_{EVAP} , the latter of which promotes denser surface water. Although SS burden is an important contributor to BMB North Atlantic AOD evolution (particularly

in the latter time periods; Supplementary Fig. 5), its effects on the AMOC are weakened due to an AMOC-SST-CLDLOW feedback.

BMB AMOC changes are largely out of phase relative to industrial aerosol-forced AMOC variations. This implies BMB acts to mute AER AMOC variations. As noted in the Introduction, CMIP6 models show anthropogenic aerosols dominate 20th century AMOC evolution, although their role may be overestimated^{25–27}. As AMOC evolution under BMB aerosols is largely out of phase with that due to industrial aerosols, our study suggests one possible cause of an excessive aerosol impact on the AMOC in CMIP6 models may be related to underestimation of the impact of BMB aerosols.

Finally, we note that continued GHG-induced climate change is expected to enhance fire weather and increase wildfire activity in the coming years^{61–64}. Under such scenarios, our results imply a possible negative feedback whereby 21st century warming-driven increases in wildfires and smoke pollution may act to mute warming-driven AMOC weakening.

Methods

CESM1-LE

CESM1-LE³⁹ includes the CAM5 atmosphere model with 30 vertical levels⁶⁵, the Parallel Ocean Program version 2 (POP2) with 60 vertical levels^{66,67}, the Community Land Model version 4 (CLM4), and the Los Alamos Sea Ice Model (CICE). All model components are at $\sim 1^\circ$ horizontal resolution. Each ensemble member has identical external forcing, including CMIP5 historical forcings from 1920–2005⁵⁹ and Representative Concentration Pathway 8.5 (RCP8.5)⁶⁸ from 2006 onwards. The first all-forcing ensemble member began in 1850 from year 401 of a long preindustrial control (PIC) simulation. All other ensemble members are branched from this first member in 1920, after the application of a small random perturbation to their initial atmospheric temperature fields (known as a “micro-perturbation”). Thus, the ensemble spread results from internally generated climate variability alone; however, CESM1-LE does not sample internal climate variability resulting from differing ocean states.

We note a few additional aspects of CESM1-LE that are important for this study. CESM1 North Atlantic multidecadal climate variability (including the AMOC) is weaker than observed, which has been related to weak North Atlantic Oscillation (NAO) variability⁶⁹. Furthermore, the climatological present-day (2005–2018) AMOC strength (calculated as the maximum stream function below 500 m at 26°N in the Atlantic Ocean) in CESM1 is 20.8 Sv, which is larger than that observed by the RAPID array at 17.5 Sv (interannual standard deviation of 1.4 Sv). We also note that the relative coarse ocean resolution (an issue with all current global climate models, particularly those integrated over long time periods with multiple ensemble members) necessitates the use of parameterizations (e.g., to resolve sub-grid scale flow, including eddy-induced and submesoscale advection). Studies with higher-resolution ocean models⁷⁰ show that the AMOC and associated northward heat transport tend to increase in strength at higher horizontal model resolution, and the AMOC declines more quickly in future projections. Both low- and high-resolution models, however, still have biases and it is not clear which biases are most important to the AMOC strength and response to external forcings⁷¹. Nonetheless, the relative coarse ocean resolution of CESM1-LE leads to additional uncertainties and caveats in our study.

CESM1 aerosols are treated using the Modal Aerosol Model version 3 (MAM3)⁷², which provides internally mixed representations of number concentrations and mass for Aitken, accumulation and coarse aerosol modes. CESM1 includes both aerosol radiation and aerosol cloud interactions, and has an aerosol effective radiative forcing (ERF) on the high-end⁷³ at $\sim -1.37 \text{ W m}^{-2}$, but this falls within recent $1-\sigma$ uncertainty estimates⁷⁴ of ~ -1.60 to -0.75 W m^{-2} . The total aerosol ERF, including that due to biomass burning aerosol, exhibits uncertainty due to emissions, optical properties, injection height and mixing state^{74–78}. For example, a recent study showed that biomass burning aerosol in most climate models is too absorbing⁷⁸.

SDF Calculation

To help understand the mechanisms associated with changes in the buoyancy-driven AMOC, we calculate the surface density flux (SDF). SDF indicates the loss or gain of density (buoyancy) at the ocean surface due to thermal (radiation, sensible and latent heat) and haline (sea-ice melting/freezing, brine rejection, precipitation minus evaporation) exchanges^{26,46,47}. An increase in North Atlantic SDF is associated with the strengthening of the AMOC; a decrease in SDF is

associated with the weakening of the AMOC²⁶. Surface density flux is defined as:

$$SDF = -\alpha \frac{SHF}{c_p} - \rho(0, SST) \beta \frac{SFWF \times SSS}{1 - SSS}, \quad (1)$$

where c_p , SST, and SSS are the specific heat capacity and sea surface temperature and salinity, respectively; α and β are thermal expansion and haline contraction coefficients; and $\rho(0, SST)$ is the density of freshwater with a salinity of zero and the temperature of SST. SHF represents the net surface heat flux into the ocean (positive downward), which is estimated as a sum of shortwave (SW) and longwave (LW) radiation, sensible (SHFLX) and latent (LHFLX) heat fluxes, and heat fluxes from sea ice melting and other minor sources. SFWF represents net surface freshwater flux into the ocean (positive downward) and is estimated as precipitation + runoff + ice melting – evaporation. The first term $-\alpha \frac{SHF}{c_p}$ represents the thermal contribution (TSDF); the second term $-\rho(0, SST) \beta \frac{SFWF \times SSS}{1 - SSS}$ represents the haline contribution (SSDF) to the density flux.

In this study, the North Atlantic is defined as $30\text{--}65^\circ\text{N}$; $0\text{--}80^\circ\text{W}$. North Atlantic time series (e.g., SDF) are based on area-weighted averages over this region. The North Atlantic region is used to investigate the initiators of AMOC changes (e.g., drivers of the trend reversal). An additional region, the subpolar North Atlantic (SPNA), is defined from $45\text{--}65^\circ\text{N}$; $0\text{--}80^\circ\text{W}$. This latter region is where the AMOC feedback are strongest, and hence, the SPNA is used to investigate AMOC feedback.

Heat and salinity budget calculations

Although the above surface density flux calculation, including both TSDF and SSDF and their components, is useful to understand drivers of AMOC changes, SDF only captures surface processes and does not directly quantify other potentially important processes, including for example salinity/heat transport or mixing by the ocean. Thus, to more rigorously quantify AMOC feedbacks, we perform heat and salinity budget calculations. The heat budget at a particular level can be written as⁷⁹:

$$\rho_0 c_p \frac{\partial \theta}{\partial t} = \rho_0 c_p \left[-\nabla \cdot (\mathbf{u}\theta) + \frac{\partial}{\partial z} \kappa \left(\frac{\partial \theta}{\partial z} - \Gamma \right) + HDIF_T \right], \quad (2)$$

where θ is potential temperature; c_p is the specific heat capacity of sea water; ρ_0 is a reference sea water density; ∇ is the 3-dimensional gradient operator; \mathbf{u} is the 3-dimensional Eulerian-mean velocity; κ is the vertical diffusivity; $\kappa\Gamma$ is the KPP (K-profile parameterization) counter-gradient flux of temperature; and HDIF_T is horizontal diffusion, which includes eddy-induced⁸⁰ and sub-mesoscale⁸¹ advection. Vertically integrating to a depth H (in our case, 100 m) and rewriting yields:

$$\rho_0 c_p \int_{-H}^0 \frac{\partial \theta}{\partial t} dz = \rho_0 c_p \int_{-H}^0 \left[-\nabla \cdot (\mathbf{u}\theta) + HDIF_T \right] dz + (SHF - SHF_{QSW}) - \kappa \left(\frac{\partial T}{\partial z} - \Gamma \right)_{-H} - (QSW_{3D})_{-H}, \quad (3)$$

where SHF is the surface heat flux, defined as the sum of net surface shortwave and longwave radiation fluxes as well as latent and sensible heat fluxes, SHF_{QSW} is the surface shortwave heat flux, and QSW_{3D} is the penetrative heat flux, accounting for the absorption of shortwave radiation at depth H. Eq. (3) can be re-written as:

$$OHS = OHFC + HHDF + SHF + HVMIX \quad (4)$$

where OHS is the ocean heat storage (i.e., ocean temperature tendency), OHFC is the ocean heat flux convergence by the resolved (Eulerian-mean) flow (i.e., $\rho_0 c_p \int_{-H}^0 -\nabla \cdot (\mathbf{u}\theta) dz$ where $\mathbf{u}\theta$ is the 3D heat transport by the resolved flow), HHDF is the heat flux due to horizontal diffusion (including eddy-induced and submesoscale advection), HVMIX is the heat flux due to

vertical mixing and SHF is again the surface heat flux (which includes SHF_{QSW}, as testing showed negligible solar penetration below 100 m).

As opposed to showing heat fluxes, we convert solar fluxes (units of W m⁻²) to a temperature flux (units of °C·cm s⁻¹) before vertical integration using CESM's "hflux_factor", which is equal to $\frac{1000}{(\rho_0 c_p)}$ or 2.44e⁻⁵. The components of our heat budget analysis therefore have units of temperature per unit time (i.e., K yr⁻¹).

In a similar manner, the salinity budget (after vertically integrating to a depth H) can written as:

$$\frac{\partial S}{\partial t} = OSFC + SHDIF + SSF + SV MIX \quad (5)$$

where $\frac{\partial S}{\partial t}$ is the ocean salinity tendency, OSFC is the ocean salinity flux convergence by the resolved (Eulerian-mean) flow (i.e., $\int_{-H}^0 -\nabla \cdot (\mathbf{u}S) \partial z$ where $\mathbf{u}S$ is the 3D salinity transport by the resolved flow), SHDIF is the salinity flux due to horizontal diffusion (including eddy-induced and submesoscale advection), SVMIX is the salinity flux due to vertical mixing and SSF is the surface salinity flux, estimated as the surface freshwater flux (SFWF) multiplied by $-34.7/1000$, where 34.7 represents a reference salinity⁸ and 1000 kg m⁻³ is the density of freshwater.

All terms on the right-hand side of the heat and salinity budget equations are available for CESM1-LE and they are exact (e.g., covariance terms are accumulated each time step and averaged at the end of each month). For example, we use the CESM variables UET (flux of heat in grid-x direction), VNT (flux of heat in grid-y direction) and WTT (heat flux across top face) to calculate OHFC. Each of these terms have units of °C s⁻¹. Similarly, we use the CESM variables UES (salt flux in grid-x direction), VNS (salt flux in grid-y direction) and WTS (salt flux across the top face). Each of these terms have units of g kg⁻¹ s⁻¹. The tendency term is estimated as the difference between monthly ocean temperatures or salinity (e.g., using centered finite differencing).

These budget analyses used the Python packages POP-tools and xgcm, which facilitate such calculations on the CESM ocean (POP) grid. A detailed description on our methodology to calculate the heat (and indirectly the salinity) budget can be found in ref. 82. We note that this example is for a high-resolution version of POP2 (0.1° horizontal resolution). As such, we have added the additional variables necessary for the lower resolution of our POP2 simulations, which includes adding "HDIFB_TEMP" to the horizontal diffusion term of the heat budget analysis and "HDIFB_SALT" to the horizontal diffusion term of the salt budget analysis. These terms represent the tendency from lateral mixing through the bottom of the cell. Thus, horizontal diffusion (i.e., HHDF and SHDIF in Eq. (4) and (5), respectively) is based on 3 terms, including the horizontal diffusive flux in grid-y direction, the horizontal diffusive flux in grid-x direction and the horizontal diffusive flux across the bottom face (terms have units of °Cs⁻¹ and g kg⁻¹ s⁻¹ for heat and salt budgets, respectively). Additional budget terms are as described in ref. 82, including the flux across the bottom face from diabatic implicit vertical mixing (CESM POP2 variables "DIA_IMPVF_TEMP" and "DIA_IMPVF_SALT") and the tendency from KPP non-local mixing (CESM POP2 variables "KPP_SRC_TEMP" and "KPP_SRC_SALT"). Both of these terms contribute to vertical mixing (i.e., HVMIX and SVMIX in Eq. (4) and (5), respectively).

Statistical significance and regression analysis

CESM1-LE model mean annual mean time series and trends are based on the mean time series over all realizations (e.g., 20 for ALL and AER, but 15 for BMB). Trends are based on a least-squares regression and significance is based on a standard two-tailed *t*-test. Error bars (e.g., time series plots) show the 90% confidence interval, estimated as $\frac{1.65*\sigma}{\sqrt{n-1}}$ where σ is the standard deviation across realizations and n is the number of realizations. The significance of correlations (*r*) is estimated from a two-tailed *t*-test as: $t = \frac{r}{\sqrt{\frac{1-r^2}{N-2}}}$, with $N-2$ degrees of freedom. Here, N is the number of years (for a correlation over time).

We have adopted the methodology of ref. 26 of decomposing the North Atlantic climate response (e.g., SST) into an aerosol-forced component and a subsequent AMOC-related feedback component. The aerosol-forced component is obtained by regressing the North Atlantic anthropogenic aerosol burden time series (BC+POM+SO₄+SOA) onto various fields (e.g., SST). Note that we do not use AOD, since part of the AOD signal is related to sea salt (especially for BMB). We also do not use the negative of the net surface solar radiation, since this field is influenced by the AMOC (i.e., through the AMOC-SST-CLDLOW feedback) which mutes the direct influence of aerosols on surface solar radiation in the North Atlantic. Spatially-dependent regression coefficients (e.g., $\frac{\delta SST}{\delta (BC+POM+SO_4+SOA)}$), or sensitivities, are based on linear least squares regression applied to the ensemble mean annual mean. To isolate the AMOC-related feedback component, variability associated with the forced component is first removed. This is accomplished by multiplying the forced sensitivities (for a given field) by the North Atlantic anthropogenic aerosol burden time series and subtracting this quantity from the original field (i.e., SST). This yields a new field (e.g., SST_{new}), without SST variability linearly associated with the forcing. A second regression is subsequently performed, where the AMOC time series is regressed onto this new field, yielding "feedback" sensitivities (e.g., $\frac{\delta SST_{new}}{\delta AMOC}$). These feedback sensitivities are plotted (e.g., Fig. 8) and represent the AMOC feedback. We note that similar results are obtained in the subpolar North Atlantic if the AMOC time series is simply regressed onto the original field (implying AMOC feedbacks dominate the signals in the subpolar North Atlantic).

Data availability

All data used in this analysis (i.e., CESM1-LE data) can be downloaded from the Climate Data Gateway at NCAR via <https://www.earthsystemgrid.org/dataset/ucar.cgd.csm4.cesmLE.html>.

Code availability

The POP-tools Python code use to calculate the heat and salinity budgets is available at <https://github.com/NCAR/pop-tools>.

Received: 18 October 2023; Accepted: 19 February 2024;

Published online: 02 March 2024

References

1. Talley, L. D. Freshwater transport estimates and the global overturning circulation: Shallow, deep and throughflow components. *Prog. Oceanogr.* **78**, 257–303 (2008).
2. Kostov, Y., Armour, K. C. & Marshall, J. Impact of the Atlantic meridional overturning circulation on ocean heat storage and transient climate change. *Geophys. Res. Lett.* **41**, 2108–2116 (2014).
3. Marshall, J., Donohoe, A., Ferreira, D. & McGee, D. The ocean's role in setting the mean position of the Inter-Tropical Convergence Zone. *Clim. Dyn.* **42**, 1967–1979 (2014).
4. Buckley, M. W. & Marshall, J. Observations, inferences, and mechanisms of the Atlantic meridional overturning circulation: A review. *Rev. Geophys.* **54**, 5–63 (2016).
5. Trenberth, K. E., Zhang, Y., Fasullo, J. T. & Cheng, L. Observation-based estimates of global and basin ocean meridional heat transport time series. *J. Clim.* **32**, 4567–4583 (2019).
6. Rahmstorf, S. et al. Exceptional twentieth-century slowdown in the Atlantic Ocean overturning circulation. *Nat. Clim. Change* **5**, 475–480 (2015).
7. Caesar, L., Rahmstorf, S., Robinson, A., Feulner, G. & Saba, V. Observed fingerprint of the weakening Atlantic Ocean overturning circulation. *Nature* **556**, 191–196 (2018).
8. Zhu, C. & Liu, Z. Weakening Atlantic overturning circulation causes South Atlantic salinity pile-up. *Nat. Clim. Change* **10**, 998–1003 (2020).
9. Boers, N. Observation-based early-warning signals for a collapse of the Atlantic Meridional Overturning Circulation. *Nat. Clim. Change* **11**, 680–688 (2021).

10. Caesar, L., McCarthy, G. D., Thornalley, D. J. R., Cahill, N. & Rahmstorf, S. Current Atlantic Meridional Overturning Circulation weakest in last millennium. *Nat. Geosci.* **14**, 118–120 (2021).
11. Jackson, L. C. & Wood, R. A. Fingerprints for early detection of changes in the AMOC. *J. Clim.* **33**, 7027–7044 (2020).
12. Keil, P. et al. Multiple drivers of the North Atlantic warming hole. *Nat. Clim. Change* **10**, 667–671 (2020).
13. Kilbourne, K. H. et al. Atlantic circulation change still uncertain. *Nat. Geosci.* **15**, 165–167 (2022).
14. Ditlevsen, P. & Ditlevsen, S. Warning of a forthcoming collapse of the Atlantic meridional overturning circulation. *Nat. Commun.* **14**, 4254 (2023).
15. Zhao, J. & Johns, W. Wind-forced interannual variability of the Atlantic Meridional Overturning Circulation at 26.5°N. *J. Geophys. Res. Oceans* **119**, 2403–2419 (2014).
16. Jackson, L. C., Peterson, K. A., Roberts, C. D. & Wood, R. A. Recent slowing of Atlantic overturning circulation as a recovery from earlier strengthening. *Nat. Geosci.* **9**, 518–522 (2016).
17. McCarthy, G. et al. Observed interannual variability of the Atlantic meridional overturning circulation at 26.5°N. *Geophys. Res. Lett.* **39**, L19609 (2012).
18. Gregory, J. M. et al. A model intercomparison of changes in the Atlantic thermohaline circulation in response to increasing atmospheric CO₂ concentration. *Geophys. Res. Lett.* **32**, L12703 (2005).
19. Drijfhout, S. S. & Hazeleger, W. Detecting Atlantic MOC changes in an ensemble of climate change simulations. *J. Clim.* **20**, 1571–1582 (2007).
20. Cheng, W., Chiang, J. C. H. & Zhang, D. Atlantic Meridional Overturning Circulation (AMOC) in CMIP5 Models: RCP and Historical Simulations. *J. Clim.* **26**, 7187–7197 (2013).
21. Weijer, W., Cheng, W., Garuba, O. A., Hu, A. & Nadiga, B. T. CMIP6 models predict significant 21st century decline of the Atlantic Meridional Overturning Circulation. *Geophys. Res. Lett.* **47**, e2019GL086075 (2020).
22. Delworth, T. L., Ramaswamy, V. & Stenchikov, G. L. The impact of aerosols on simulated ocean temperature and heat content in the 20th century. *Geophys. Res. Lett.* **32**, L24709 (2005).
23. Delworth, T. L. & Dixon, K. W. Have anthropogenic aerosols delayed a greenhouse gas-induced weakening of the North Atlantic thermohaline circulation? *Geophys. Res. Lett.* **33**, L02606 (2006).
24. Menary, M. B. et al. Mechanisms of aerosol-forced AMOC variability in a state of the art climate model. *J. Geophys. Res. Oceans* **118**, 2087–2096 (2013).
25. Menary, M. B. et al. Aerosol-forced AMOC changes in CMIP6 historical simulations. *Geophys. Res. Lett.* **47**, e2020GL088166 (2020).
26. Hassan, T., Allen, R. J., Liu, W. & Randles, C. A. Anthropogenic aerosol forcing of the Atlantic meridional overturning circulation and the associated mechanisms in CMIP6 models. *Atmos. Chem. Phys.* **21**, 5821–5846 (2021).
27. Robson, J. et al. The role of anthropogenic aerosol forcing in the 1850–1985 strengthening of the AMOC in CMIP6 historical simulations. *J. Clim.* **35**, 6843–6863 (2022).
28. Li, S., Liu, W., Allen, R. J., Shi, J.-R. & Li, L. Ocean heat uptake and interbasin redistribution driven by anthropogenic aerosols and greenhouse gases. *Nat. Geosci.* **16**, 695–703 (2023).
29. Eyring, V. et al. Overview of the Coupled Model Intercomparison Project Phase 6 (CMIP6) experimental design and organization. *Geosci. Model Dev.* **9**, 1937–1958 (2016).
30. Zhang, J. et al. The role of anthropogenic aerosols in the anomalous cooling from 1960 to 1990 in the CMIP6 Earth system models. *Atmos. Chem. Phys.* **21**, 18609–18627 (2021).
31. Ma, X., Liu, W., Allen, R. J., Huang, G. & Li, X. Dependence of regional ocean heat uptake on anthropogenic warming scenarios. *Sci. Adv.* **6**, eabc0303 (2020).
32. Hassan, T. et al. Air quality improvements are projected to weaken the Atlantic meridional overturning circulation through radiative forcing effects. *Commun. Earth Environ.* **3**, 149 (2022).
33. Gillett, N. P. et al. The Detection and Attribution Model Intercomparison Project (DAMIP v1.0) contribution to CMIP6. *Geosci. Model Dev.* **9**, 3685–3697 (2016).
34. Fasullo, J. T. et al. Spurious late historical-era warming in CESM2 driven by prescribed biomass burning emissions. *Geophys. Res. Lett.* **49**, e2021GL097420 (2022).
35. DeRepentigny, P. et al. Enhanced simulated early 21st century Arctic sea ice loss due to CMIP6 biomass burning emissions. *Sci. Adv.* **8**, eab02405 (2022).
36. Heyblom, K. B., Singh, H. A., Rasch, P. J. & DeRepentigny, P. Increased variability of biomass burning emissions in CMIP6 amplifies hydrologic cycle in the CESM2 Large Ensemble. *Geophys. Res. Lett.* **49**, e2021GL096868 (2022).
37. Kim, J.-E. et al. Interannual fires as a source for subarctic summer decadal climate variability mediated by permafrost thawing. *npj Clim. Atmos. Sci.* **6**, 84 (2023).
38. Yamaguchi, R. et al. Persistent ocean anomalies as a response to northern hemisphere heating induced by biomass burning variability. *J. Clim.* **36**, 8225–8241 (2023).
39. Kay, J. E. et al. The Community Earth System Model (CESM) Large Ensemble Project: A community resource for studying climate change in the presence of internal climate variability. *Bull. Amer. Meteorol. Soc.* **96**, 1333–1349 (2015).
40. Deser, C. et al. Isolating the evolving contributions of anthropogenic aerosols and greenhouse gases: A new CESM1 large ensemble community resource. *J. Clim.* **33**, 7835–7858 (2020).
41. Rodgers, K. B. et al. Ubiquity of human-induced changes in climate variability. *Earth Syst. Dyn.* **12**, 1393–1411 (2021).
42. Simpson, I. R. et al. The CESM2 single-forcing large ensemble and comparison to CESM1: Implications for experimental design. *J. Clim.* **36**, 5687–5711 (2023).
43. Kawase, M. Establishment of deep ocean circulation driven by deep-water production. *J. Phys. Oceanogr.* **17**, 2294–2317 (1987).
44. Johnson, H. L. & Marshall, D. P. A theory for the surface Atlantic response to thermohaline variability. *J. Phys. Oceanogr.* **32**, 1121–1132 (2002).
45. Zhang, R. Latitudinal dependence of Atlantic meridional overturning circulation (AMOC) variations. *Geophys. Res. Lett.* **37**, L16703 (2010).
46. Liu, W., Xie, S.-P., Liu, Z. & Zhu, J. Overlooked possibility of a collapsed Atlantic Meridional Overturning Circulation in warming climate. *Sci. Adv.* **3**, e1601666 (2017).
47. Liu, W., Fedorov, A. & Séville, F. The mechanisms of the Atlantic Meridional Overturning Circulation slowdown induced by Arctic sea ice decline. *J. Clim.* **32**, 977–996 (2019).
48. Roberts, C. D. et al. Atmosphere drives recent interannual variability of the Atlantic meridional overturning circulation at 26.5°N. *Geophys. Res. Lett.* **40**, 5164–5170 (2013).
49. Delworth, T. L. & Zeng, F. The Impact of the North Atlantic Oscillation on climate through its influence on the atlantic meridional overturning circulation. *J. Clim.* **29**, 941–962 (2016).
50. Delworth, T. L. et al. The Central Role of Ocean dynamics in connecting the North Atlantic oscillation to the extratropical component of the Atlantic Multidecadal Oscillation. *J. Clim.* **30**, 3789–3805 (2017).
51. Wilcox, L. J. et al. Mechanisms for a remote response to Asian anthropogenic aerosol in boreal winter. *Atmos. Chem. Phys.* **19**, 9081–9095 (2019).
52. Dittus, A. J., Hawkins, E., Robson, J. I., Smith, D. M. & Wilcox, L. J. Drivers of recent north Pacific decadal variability: The role of aerosol forcing. *Earth's Future* **9**, e2021EF002249 (2021).

53. Dow, W. J., Maycock, A. C., Lofverstrom, M. & Smith, C. J. The effect of anthropogenic aerosols on the Aleutian low. *J. Clim.* **34**, 1725–1741 (2021).

54. Allen, R. J. & Zhao, X. Anthropogenic aerosol impacts on Pacific Coast precipitation in CMIP6 models. *Environ. Res.: Clim.* **1**, 015005 (2022).

55. Klein, S. A. & Hartmann, D. L. The seasonal cycle of low stratiform clouds. *J. Clim.* **6**, 1587–1606 (1993).

56. Wood, R. & Bretherton, C. S. On the relationship between stratiform low cloud cover and lower-tropospheric stability. *J. Clim.* **19**, 6425–6432 (2006).

57. Stommel, H. Thermohaline convection with two stable regimes of flow. *Tellus* **13**, 224–230 (1961).

58. Rahmstorf, S. On the freshwater forcing and transport of the Atlantic thermohaline circulation. *Clim. Dyn.* **12**, 799–811 (1996).

59. Lamarque, J. F. et al. Historical (1850–2000) gridded anthropogenic and biomass burning emissions of reactive gases and aerosols: methodology and application. *Atmos. Chem. Phys.* **10**, 7017–7039 (2010).

60. van Marle, M. J. E. et al. Historic global biomass burning emissions for CMIP6 (BB4CMIP) based on merging satellite observations with proxies and fire models (1750–2015). *Geosci. Model Dev.* **10**, 3329–3357 (2017).

61. Pechony, O. & Shindell, D. T. Driving forces of global wildfires over the past millennium and the forthcoming century. *Proc. Natl. Acad. Sci. USA* **107**, 19167–19170 (2010).

62. Abatzoglou, J. T., Williams, A. P. & Barbero, R. Global emergence of anthropogenic climate change in fire weather indices. *Geophys. Res. Lett.* **46**, 326–336 (2019).

63. United Nations Environment Programme. Spreading like Wildfire – The Rising Threat of Extraordinary Landscape Fires, 126 pp. (2022).

64. Allen, R. J., Gomez, J., Horowitz, L. W. & Shevliakova, E. Enhanced future vegetation growth with elevated carbon dioxide concentrations could increase fire activity. *Commun. Earth Environ.* **5**, 54 (2024).

65. Neale, R. B. et al. Description of the NCAR Community Atmosphere Model (CAM 5.0). NCAR/TN-486+STR, 274 pp., National Center for Atmospheric Research (2012).

66. Smith, R. et al. The Parallel Ocean Program (POP) Reference Manual: Ocean Component of the Community Climate System Model (CCSM) and Community Earth System Model (CESM). LAUR-10-01853, Los Alamos National Laboratory, pp 140 (2010).

67. Danabasoglu, G. et al. The CCSM4 ocean component. *J. Clim.* **25**, 1361–1389 (2012).

68. Meinshausen, M. et al. The RCP greenhouse gas concentrations and their extensions from 1765 to 2300. *Clim. Change* **109**, 213 (2011).

69. Kim, W. M., Yeager, S., Chang, P. & Danabasoglu, G. Low-frequency north Atlantic climate variability in the Community Earth System Model Large Ensemble. *J. Clim.* **31**, 787–813 (2018).

70. Roberts, M. J. et al. Sensitivity of the Atlantic Meridional overturning circulation to model resolution in CMIP6 HighResMIP simulations and implications for future changes. *J. Adv. Model. Earth Syst.* **12**, e2019MS002014 (2020).

71. Jackson, L. C. et al. Impact of ocean resolution and mean state on the rate of AMOC weakening. *Clim. Dyn.* **55**, 1711–1732 (2020).

72. Liu, X. et al. Toward a minimal representation of aerosols in climate models: description and evaluation in the Community Atmosphere Model CAM5. *Geosci. Model Dev.* **6**, 709–739 (2012).

73. Zelinka, M. D., Andrews, T., Forster, P. M. & Taylor, K. E. Quantifying components of aerosol-cloud-radiation interactions in climate models. *J. Geophys. Res. Atmos.* **119**, 7599–7615 (2014).

74. Bellouin, N. et al. Bounding global aerosol radiative forcing of climate change. *Rev. Geophys.* **58**, e2019RG000660 (2020).

75. Myhre, G. et al. Anthropogenic and Natural Radiative Forcing. In: Climate Change 2013: The Physical Science Basis. Contribution of Working Group I to the Fifth Assessment Report of the Intergovernmental Panel on Climate Change [Stocker, T.F., D. Qin, G.-K. Plattner, M. Tignor, S.K. Allen, J. Boschung, A. Nauels, Y. Xia, V. Bex and P.M. Midgley (eds.)]. Cambridge University Press, Cambridge, United Kingdom and New York, NY, USA (2013).

76. Myhre, G. et al. Radiative forcing of the direct aerosol effect from AeroCom Phase II simulations. *Atmos. Chem. Phys.* **13**, 1853–1877 (2013).

77. Bond, T. C. et al. Bounding the role of black carbon in the climate system: A scientific assessment. *J. Geophys. Res. Atmos.* **118**, 5380–5552 (2013).

78. Brown, H. et al. Biomass burning aerosols in most climate models are too absorbing. *Nat. Commun.* **12**, 277 (2021).

79. Small, R. J., Bryan, F. O., Bishop, S. P., Larson, S. & Tomas, R. A. What drives upper-ocean temperature variability in coupled climate models and observations? *J. Clim.* **33**, 577–596 (2020).

80. Gent, P. R. & McWilliams, J. C. Isopycnal mixing in ocean circulation models. *J. Phys. Oceanogr.* **20**, 150–155 (1990).

81. Fox-Kemper, B., Ferrari, R. & Hallberg, R. Parameterization of mixed layer eddies. Part I: Theory and diagnosis. *J. Phys. Oceanogr.* **38**, 1145–1165 (2008).

82. UCAR. POP-tools: Tools to support analysis of POP2-CESM model solutions with xarray. <https://pop-tools.readthedocs.io/en/latest/>.

Acknowledgements

R. J. A. and W. L. are supported by NSF grant AGS-2153486.

Author contributions

R.J.A. designed the study and performed data analyses. C.V. and E.Y. performed data analysis. W.L. advised on methods. All authors discussed the results and contributed to the writing of the manuscript.

Competing interests

The authors declare no competing interests.

Additional information

Supplementary information The online version contains supplementary material available at <https://doi.org/10.1038/s41612-024-00602-8>.

Correspondence and requests for materials should be addressed to Robert J. Allen.

Reprints and permissions information is available at <http://www.nature.com/reprints>

Publisher's note Springer Nature remains neutral with regard to jurisdictional claims in published maps and institutional affiliations.

Open Access This article is licensed under a Creative Commons Attribution 4.0 International License, which permits use, sharing, adaptation, distribution and reproduction in any medium or format, as long as you give appropriate credit to the original author(s) and the source, provide a link to the Creative Commons licence, and indicate if changes were made. The images or other third party material in this article are included in the article's Creative Commons licence, unless indicated otherwise in a credit line to the material. If material is not included in the article's Creative Commons licence and your intended use is not permitted by statutory regulation or exceeds the permitted use, you will need to obtain permission directly from the copyright holder. To view a copy of this licence, visit <http://creativecommons.org/licenses/by/4.0/>.

© The Author(s) 2024